Wildland-Urban Interface Fire Exposure Assessment Using Remote-Sensing Framework

by

Mohammad Afaghi

A thesis submitted in partial fulfillment of the requirements for the degree of

Master of Science

in

Structural Engineering

Department of Civil and Environmental Engineering
University of Alberta

© Mohammad Afaghi, 2024

Abstract

Wildfires occurring in proximity to urban areas pose a potential risk to the safety and well-being of the population, while also carrying the potential for substantial economic damage through the destruction of infrastructure and private property. Canada, given its unique geographical and climatic conditions, is among the countries facing significant wildfire challenges. Alberta, in particular, has recorded the highest number of wildfires compared to other Canadian provinces, making it increasingly susceptible to fires in Wildland Urban Interface (WUI) regions. These are regions where natural vegetation intersects or mixes with structures, and where the population is growing. Due to the vastness of human settlements and infrastructure needed to be monitored, the precision of fire risk assessment plays a crucial role in effective fire management. It is therefore necessary to advance a framework to determine fire behaviour in WUI. In this study I focus on fire exposure within the WUI, and a building in the City of Edmonton serves as a case study. Studies suggest that the characteristics of a small portion of the WUI, known as the Home Ignition Zone (HIZ), are a significant factor in determining the level of exposure in wildfire ignition. The primary goal of this study is to develop an automated method that aligns with national guidelines for characterizing vegetation land cover as various fuel types. This method employs convolutional neural networks and incorporates topographical factors, including the identification of ignition zones near buildings and accounting for slope effects. These parameters are valuable for pinpointing potentially high-risk individual HIZ or clusters of HIZ in a neighborhood. Summertime RGB satellite imagery is utilized to detect and categorize tree canopies and grass-covered areas, while wintertime satellite imagery is employed to address the challenge of distinguishing between conifer and deciduous trees, two fuel types with differing fire behaviours. The methods described in this study can be

combined with in situ data collection and extended for use in different regions to inform hazard mitigation plans.

Acknowledgements

First, I would like to express my profound appreciation to my supervisors, Dr. Mustafa Gul and Dr. Nima Shirzad Ghaleroudkhani, for their guidance and encouragement throughout the period of actualizing this thesis. Their supervision within the period of my studies has reoriented my solution-finding abilities. Their expertise, knowledge, and dedication were instrumental in the success of my research project.

It is important to acknowledge the contributions of all members of the research group. A great gratitude also goes to Daniel Jozi and Asdrubal Cheng Cen. Without their hard work, dedication, and collaboration, the project would not have been successful. Each member brought unique skills and expertise to the team, which helped us to address the research questions and achieve our goals. Working with such a talented and supportive team was a pleasure, and I feel fortunate to have been part of it. The collaborative nature of our work allowed us to learn from each other, share ideas, and overcome obstacles together.

Funding support from Alberta Ecotrust and the City of Edmonton under the Cities-IPCC Grant Program (Grant 2021-I-72-IPCC) is gratefully acknowledged. In addition, we are grateful to AI4Society at the University of Alberta for their partial financial support of this research.

I want to express my gratitude to my family for their unwavering support throughout my master's thesis journey. Their encouragement, patience, and understanding were instrumental in helping me stay focused and motivated during the project.

Table of Contents

List of Tables

List of Figures

Notations

Symbol	=	Definition
cm	=	Centimeter
km	=	Kilometer
km^2	=	Square kilometer
m	=	Meter
nm	=	nanometer
y_t	=	Ground truth
y_p	=	Predicted output
°C	=	Degree Celsius

Abbreviation	=	Description
ANN	=	Artificial neural network
CHM	=	Canopy height model
CNN	=	Convolutional neural network
FBP	=	Forest fire behavior prediction
GPS	=	Global positioning system
GSV	=	Google street view
HIZ	=	Home ignition zone
Lidar	=	Light detection and ranging
MSE	=	Mean squared error
NDVI	=	Normalized difference vegetation index
NIR	=	Near-infrared
NRC	=	National research council of Canada
RGB	=	Red, green, and blue
SVM	=	Support vector machine
UAV	=	Unmanned aerial vehicle
WUI	=	Wildland urban interface

Chapter 1

Introduction

Creating accurate vegetation maps is critical for urban planners to optimize climate change adaptation and urban ecosystem services. Climate change is a significant global issue that poses challenges for many countries worldwide. In Canada, air temperatures increased by 1.5°C between 1950 and 2010, which is twice the global average increase during that time period, according to observational records [1]. This suggests that Canada is particularly vulnerable to climate change impacts. Several studies have shown that climate change is exacerbating the risk of wildfires in Canada. For example, researchers at Environment and Climate Change Canada have found that the hot and dry weather caused by greenhouse gas emissions has increased wildfire activity in British Columbia up to fourfold and increased the area burnt by wildfires up to elevenfold [2]. The scientific community predicts that, due to climate change, Canada's wildland areas will experience more dry fuels that are prone to burning, more frequent lightning strikes that can initiate fires, and more frequent and intense dry, windy weather that can spread the flames [3]. Climate change impact assessment studies, such as Wotton et al. [4], suggest that future wildfire occurrences in Canada could rise by as much as 140% as a result of climate change.

As an example of a recent wildfire in Alberta, the wildfire season of 2023 can be mentioned, setting new records for the extent of devastation compared to pre-

vious years. Spanning from March 1 through October 31, the season saw 1,092 wildfires, which affected an extraordinary area of about 2.2 million hectares, a size nearly tenfold the average of past years [5]. Although the count of wildfires aligned with the five-year average, the sheer magnitude of land affected indicated a significant escalation in fire severity. This challenging period led to the evacuation of 48 communities, impacting the lives of more than 38,000 individuals [5]. More specifically, in the City of Edmonton, a wildfire struck several communities west of Edmonton in April 2023, leading to a widespread evacuation in some communities of the region and causing significant disruption to the affected community [6]. The wildfire in west of Edmonton was fueled by prolonged drought conditions, high temperatures, and strong winds, which created ideal conditions for the rapid spread of flames. The wildfire event in the area and the subsequent evacuation underscore the importance of mapping hazard zones for urban areas to mitigate the impact of fires.

Wildfires are a significant cause for concern in the Wildland-Urban Interface (WUI) [7–9]. Urban areas, particularly those situated close to wildlands, are becoming more vulnerable as they are located within or near densely forested areas. Moreover, structures such as houses can pose a significant threat by adding to the overall fuel load and creating a domino effect, with the fire spreading to the surrounding vegetation and rapidly intensifying in strength. A recent example is the fire that occurred in the city of Lytton, British Columbia on June 30, 2021, which destroyed 151 buildings and claimed the lives of two people [10]. In another example, the 2018 Camp fire, which occurred in WUI area, resulted in the destruction of more than 18,000 buildings and claimed the lives of 85 individuals [11]. Hence, it is vital to regularly inspect and update the boundaries and characteristics of WUI regions, particularly at the level of individual buildings.

Research into wildfire risk in the WUI usually involves modeling potential wildfire intensity or exposure using various factors like vegetation, topography, and housing density [12–14]. While these large-scale assessments help with broad spatial comparisons, they have a significant drawback: they cannot accurately predict wildfire risk at the level of individual buildings or neighborhoods. This limitation arises because the threat to structures from wildfires is heavily influenced

by local factors rather than broader landscape characteristics [15]. Both modeling and experimental investigations have demonstrated that the potential for structure ignition by wildfires is significantly influenced by a specific portion of the WUI situated within 30-100 meters of buildings. This critical area is commonly referred to as the Home Ignition Zone (HIZ) [8, 16, 17]. The likelihood of ignition primarily depends on how wildfires behave within the HIZ, which depends on factors such as fuel types and slope [18, 19]. These insights have been incorporated into guidelines for mitigating ignition hazards by organizations like the National Research Council Canada [20]. Mapping hazards within the HIZ would allow authorities to assess the vulnerability of the urban area to wildfires and make informed decisions regarding land management practices and building codes.

Compared to natural vegetation types like forests and rangelands, urban areas tend to have fragmented vegetation cover. This is due to the irregular and diverse nature of the urban landscape, which has made accurately mapping and identifying vegetation cover more difficult [21]. Urbanization, land use changes, and human activities contribute to the patchy nature of urban vegetation, which has varying types of vegetation distributed throughout the landscape. To address these challenges, the field of remote sensing has been actively exploring and developing methods to effectively map and extract land use types over urban vegetation cover. Remote sensing data, which involves collecting data about the Earth's surface from airborne or satellite sensors, has become a widely used method for vegetation mapping in various environments [22]. Remote sensing data can provide detailed and precise information on land cover types and vegetation present, enabling urban planners to identify areas in need of vegetation and to plan more efficiently for the future. However, due to the complexity of the urban environment, researchers have had to develop innovative techniques and approaches to ensure the accuracy and reliability of their findings.

Earth's remote sensing has evolved significantly, beginning with aerial photography in the 19th century and advancing to modern UAV-based remote sensing. Today, remote sensing predominantly implies satellite remote sensing, which began in 1972 with the launch of Landsat-1 for civilian use [23]. Since then, satellite remote sensing has witnessed numerous advancements, including the introduction

of optical and radar systems with higher spatial resolution, the development of hyperspectral sensors, and the creation of valuable derivatives like the digital elevation model [23]. This progression has been pivotal in the field's capability to map and extract land use types in urban vegetation cover effectively. The aforementioned methods laid the foundation for understanding urban landscapes and classifying various types of vegetation cover. However, the increasing complexity of urban environments has required more advanced and refined techniques.
The emergence of deep learning, a branch of machine learning, marked a significant advancement in this evolution. Deep learning involves the use of neural networks to process information [24]. Convolutional Neural Networks (CNNs), which are a subcategory of deep learning algorithms, excel at processing images, videos, and audio [25, 26]. They have the ability to classify the content of an image or mask objects at a pixel level, a process known as semantic segmentation. In remote sensing, the term "segmentation" traditionally refers to dividing the image into groups of pixels that share a similar spectral signature, which are then classified by a traditional machine learning tool such as a support vector machine, based on their color or other characteristics. On the other hand, "segmentation" in computer vision refers to the masking of entire physical objects. CNNs can perform object delineation and classification simultaneously, unlike traditional methods that involve multiple steps. As such, CNNs can be used to segment remote sensing imagery, which is one of the topics covered in the presented work.

1.1 Objectives and Scope

The objective of this thesis is to develop a methodology using satellite imagery, specifically through Google Engine, to assess the level of heat radiation that can be created by a potential fire in urban areas, with a particular focus on a building in Edmonton. This study aims to assess the potential of satellite imagery in identifying fire exposure levels in urban areas. It will examine key factors such as local topography, including slope, and the proximity of fuel types near buildings by utilizing artificial intelligence techniques. Employing a variety of satellite data, the study will analyze landscape characteristics and fuel types in the area. The anticipated outcomes, including a detailed fire exposure map in accordance with

current wildfire guidelines, are expected to contribute to the effectiveness of wildfire management strategies in urban environments, enhancing public safety and reducing property damage. This approach offers the possibility of automating the heat exposure assessment process in a significantly shorter time-frame compared to on-site inspections, which not only demand considerable time but also require extensive human resources.

1.1.1 Limitations and Assumptions

The methodology focuses primarily on assessing heat radiation exposure and has limitations in incorporating ember transfer exposure. Furthermore, incorporating weather factors, including wind speed, direction, and moisture levels, into the analysis is challenging. These elements, being key components of the fire triangle, require a constantly updating system to accurately reflect real-time conditions, and integrating such dynamic data would necessitate an advanced computational framework. The reference guideline used in this study, however, do not provide a comprehensive method for including wind in the heat exposure assessment. As the study's main objective is to implement the guideline's note within a remote-sensing framework, weather-related factors, including wind, are not considered in the analysis.
This study encounters a further limitation concerning the use of satellite imagery. The assessment of heat exposure relies on mapping various fuel types, a process predominantly conducted during the summer. However, this approach presents challenges when satellite images from other seasons are used. For instance, in the winter, identifying fuels like deciduous trees, which lose their leaves, and grass areas potentially hidden under snow, becomes considerably more complex.

1.2 Thesis Structure

An overview of the thesis structure is presented below;

- **Chapter 1: Introduction**
- **Chapter 2: Background and Literature Review**
- **Chapter 3: Methodology**

- **Chapter 4: Results and Discussions**
- **Chapter 5: Conclusions and Future Work**

Chapter 2

Background and Literature Review

This chapter is divided into six sections. Section 2.1 offers an introduction to aerial imagery technologies applicable in remote sensing. Subsequently, Section 2.2 outlines the key parameters essential for understanding CNNs. Section 2.3 delves into the ignition behavior of various fuel types, such as conifer and deciduous trees, and introduces these different fuel categories as outlined in the National Guide for Wildland-Urban Interface Fires [20]. Section 2.4 then defines the factors that must be taken into account when determining priority zones. Section 2.5 explains the terminology of exposure assessment, discusses the different modes of wildfire transfer, and provides guidelines on how to take fire exposure levels into account. Section 2.6 briefly presents fire statistics for Canada and Alberta and provides an overview of the study area. Finally, Section 2.7 highlights previous studies related to WUI wildfire risk, as well as those involving aerial-based remote sensing and ground-based remote sensing.

2.1 Aerial/Satellite Imagery

Urban vegetation mapping has become more efficient and accurate due to the use of satellite and unmanned aerial vehicle (UAV) imagery [27]. This technology allows researchers to capture high-resolution images from different angles, making it easier to map urban vegetation cover.

The current space technology boasts a range of remote sensing satellites that are specialized for different applications. For the purpose of deep learning image processing, I will focus only on optical sensors, which are the most widely available and suitable. Among these, Landsat program satellites have been in orbit for several decades, enabling the study of land cover changes over time. Other significant optical remote sensing satellites include Pléiades 1A/B, the WorldView series, QuickBird, and IKONOS. These satellites orbit the earth in a sun-synchronous, poloidal trajectory at lower altitudes between 450 km and 800 km. Satellites capture images using a range of wavelengths, which are divided into multiple bands. The red, green, blue, and near-infrared (NIR) bands, covering a range of approximately 518-954 nm, are crucial for land cover classification. The difference between the red and near-infrared bands is particularly useful for determining the amount of vegetation on the ground. As an example, QuickBird and IKONOS satellites can capture images using visible and near-infrared wavelengths of light and they are useful for mapping urban vegetation cover, as they can provide images with pixel resolutions of less than a meter [21, 28].
In 2010, Google launched the Google Earth Engine (GEE), an open-source cloud-based platform for remote sensing [29]. It centralizes extensive publicly available data, enabling easy data import through user-friendly JavaScript and Python APIs. Google Earth and Maps use satellite imagery from Landsat and the higher-resolution Sentinel-2 satellite, along with aerial photography, for detailed mapping. Sentinel-2, operated by the European Space Agency, offers up to 10 meters per pixel resolution, enabling finer mapping of urban areas and small features. This is supplemented with high-resolution aerial photos for maps and 3D models [30, 31]. One of the advantages of using satellite imagery for urban vegetation mapping is its ability to cover large areas quickly and efficiently. Additionally, satellite imagery can provide data over extended periods, allowing researchers to analyze vegetation cover changes over time.

UAV imagery provides even higher resolution images and is useful for mapping small areas or capturing images of vegetation in difficult-to-reach locations. However, the use of satellite and UAV imagery has some disadvantages. Atmospheric conditions such as cloud cover and haze can reduce the quality and accuracy of these images. The cost of obtaining and processing satellite or UAV imagery can

also be high, which may limit its use in some research projects.

2.1.1 Spectral Indices

By utilizing imaging bands beyond the traditional red, green, and blue, it is possible to take advantage of the unique spectral properties of various materials. One particularly common substance found in nature is chlorophyll, which exists in multiple forms. As shown in Figure 2.1, the absorption spectra of two different types of chlorophyll, found in plants, algae, and bacteria, can be utilized in remote sensing applications.

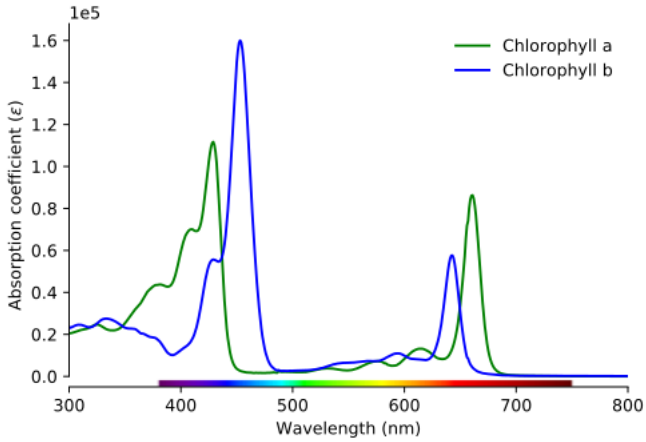

Figure 2.1: Absorption spectra of Chlorophyll A and B [32]

The absorption spectra of the two chlorophyll variants presented in Figure 2.1 indicate that they exhibit absorption maxima in the blue (430 nm, 454 nm) and red (643 nm, 662 nm) regions of the spectrum, with lower absorption observed for longer wavelengths. Since chlorophyll-rich materials absorb most blue and red light and reflect most infrared light, they appear green to the human eye. These spectral properties can be utilized to develop various indices to distinguish between different materials. For plant detection, the normalized difference vegetation index (NDVI) is the most significant index. The NDVI can be calculated as follows:

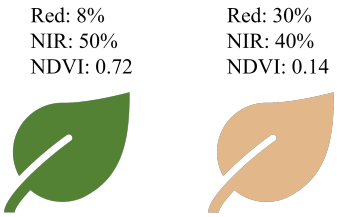

Figure 2.2: An example of Normalized Difference Vegetation Index

$$\text{NDVI} = \frac{\text{NIR - red}}{\text{NIR + red}} \tag{2.1}$$

The NDVI is a quantitative indicator that ranges between -1 and 1, where high values indicate the presence of green vegetation and low values indicate the presence of non-vegetated surfaces such as bare soil or impervious areas. Negative NDVI values can be indicative of water bodies, although the presence of algae can sometimes complicate the interpretation. While there exist numerous other indices that are traditionally employed for land cover classification, I will not delve into those in this report since my focus is on providing an overview of the NDVI for a specific region.

2.2 Convolutional Neural Network

CNN is a type of deep learning that excels in processing images, videos, and audio [25, 26]. They have the ability to classify image contents and perform pixel-level object masking, which is referred to as semantic segmentation. In computer vision, segmentation involves masking entire physical objects. The advantage of using CNNs for segmentation is that they can perform both object delineation and classification simultaneously.

2.2.1 Neural Networks

Renowned pioneers in the field of deep learning, namely LeCun, Bengio, and Hinton, provide a definition of neural networks as ”computational models that consist of multiple processing layers capable of acquiring representations of data with

varying levels of abstraction." This quote highlights four essential concepts: computational model, layer, learning, and abstraction [33]. Neural networks serve as computational models, meaning they take in an input, process it, and generate an output. The specific arrangement of components within the model determines the types of tasks it can handle. This leads to the second concept: deep learning models are constructed with layers, which in turn comprise artificial neurons. These artificial neurons are inspired by their biological counterparts, thus lending the term "neural network" its name. Every processing layer within a neural network performs a specific mathematical operation on its input. The nature of these operations relies on the connections between neurons and their respective connection strengths, known as connection weights. Given a model input x, there exists a desired network output (referred to as the ground truth) y_t, and an actual output (predicted output) y_p. Since the actual output is influenced by all the weights within the network, there exists a specific set of weights for which the predicted output y_p is closest to the desired output y_t. To discover this optimal solution, a technique known as backpropagation is employed, which corresponds to the learning process mentioned as the second last key term. As an illustration, consider an image serving as the input to such a network, with the objective of classifying the depicted content. Referring to the final key term, the network in this scenario abstracts from the specific pixel values of the image and assigns it to a category such as "car" or "tree." In the intermediate stages, the network generates "multiple levels of abstraction." For instance, it may initially create an enhanced version of the input with emphasized edges or filtered colors. However, as the layers progress, the output becomes increasingly challenging for humans to interpret, leading to criticism of neural networks for their lack of transparency [34]. The primary distinction between deep learning and traditional machine learning lies in how the models derive their features for prediction. In traditional machine learning, humans manually craft the features used by the model, making them understandable and interpretable. On the other hand, in deep learning, these features are generated through the backpropagation process and numerical optimization. The term "deep learning" is indicative of the neural networks used, which can have numerous layers, allowing for the exploration of complex relationships and patterns [35]. Numerous variations of neural networks exist, but for the purpose of this thesis, my

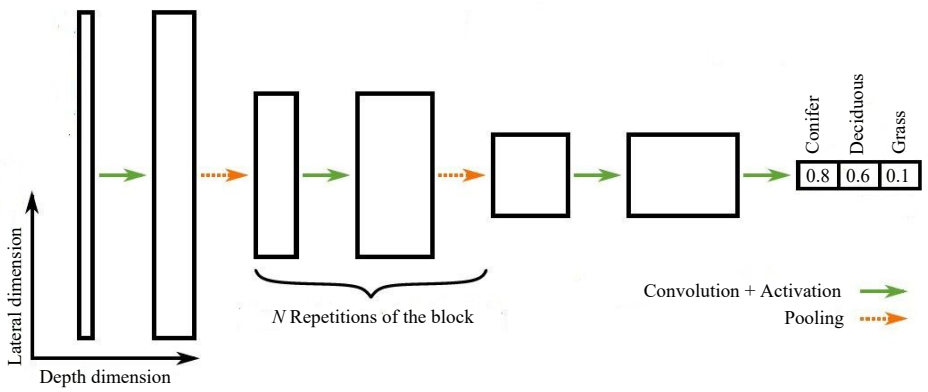

Figure 2.3: The architecture of a general fully convolutional network for classification

focus will primarily be on CNNs. CNNs are particularly well-suited for tasks such as image classification and segmentation. The provided Figure 2.3 illustrates the architecture of a typical fully convolutional network (FCN) utilized in image classification. The architecture of a general FCN for classification can be outlined as follows; initially, a convolution operation is applied to the input image, succeeded by a non-linear activation function and a pooling operation, which reduces the height and width dimensions by half. This sequence of convolution, activation, and pooling is repeated in an alternating fashion until the output becomes compact enough. Finally, a final convolution transforms the output into a vector that represents the probabilities for each class.

The network receives an image as input, typically consisting of three channels (red, green, and blue) in the depth dimension. However, in remote sensing satellite images, there can be a multitude of channels or bands. In Figure 2.3, the width and height dimensions of the image are represented as a single condensed dimension. The input image undergoes a series of operations: convolution, activation function, and pooling. This sequence is repeated until a final convolution generates a vector containing class probabilities. The convolution operation learns the necessary features for classification, the activation function introduces non-linearity crucial for the learning process, and pooling reduces the lateral dimensions while filtering out the most pertinent information. As this particular sequence is commonly found in neural network structures, these operations will be explained later in this study.

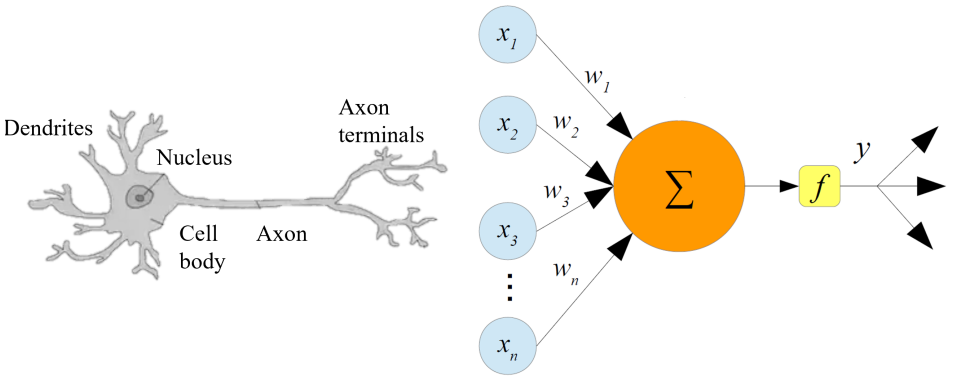

Figure 2.4: Biological and artificial neurons that share certain characteristics [36].

Neurons

The neuron serves as the fundamental operational unit within the brain. It consists of various components, including the cell body, dendrites, and axon. The dendrites act as the ”receiving end” of the neuron, while the axon functions as the ”transmitting end.” Neurons typically possess multiple dendrites, but only one axon, although exceptions exist. Synapses facilitate the connection between the axon of one neuron and the dendrites of another. These connections possess varying strengths, dictating the efficiency of signal transmission between cells. In essence, incoming signals received by the dendrites are consolidated in the cell body. If the cumulative signal surpasses a certain threshold, it is then propagated to the subsequent neuron via the axon.

For many years, researchers have been simulating this behavior through computer experiments, and one prominent outcome is the perceptron, which was invented by Rosenblatt in 1958 [37]. The perceptron is a network comprised of artificial neurons. Figure 2.4 illustrates a simplified representation of a biological neuron alongside its artificial equivalent, which forms the perception. Both biological and artificial neurons share certain characteristics. In both cases, information received from incoming axons is denoted as x_i. The strength of synaptic connections is represented by a weight parameter ω_i. To simulate the integration process within the cell body, a weighted summation is employed, followed by an activation function f, which determines whether the information is transmitted further or not. The

resulting output y corresponds to the axon's role, serving as the input for the subsequent neuron.
The artificial neuron can be mathematically represented by Equation 2.2. This equation encompasses a weighted summation of inputs, which is subsequently followed by a non-linear activation function. The activation function imitates the threshold mechanism employed by the cell body in biological neurons.

$$y = f(\sum_i \omega_i x_i + \beta_i) \tag{2.2}$$

Where the x_i in input to the neuron, ω_i is the weight parameter, β_i is the additive bias, f is the activation function, and y is the neuron output. The connection weights ω_i undergo a learning process known as backpropagation. Neurons can be combined to form layers, and by connecting these layers sequentially, the network can perform basic logic operations. As the complexity of the network increases, it becomes capable of handling more intricate tasks.

Convolutional layers

The fundamental operation of convolution serves as the key component of CNNs, hence their name. When dealing with discrete raster data, like images, convolution involves two inputs: the image I and a kernel K, which is applied to the image. In this context, both the image and the kernel are three-dimensional arrays. The image, denoted as I, has dimensions of H pixels in height, W pixels in width, and C channels in depth. Similarly, the kernel is represented as a matrix with dimensions $H_k \times W_k \times C$, ensuring that the image and kernel share the same number of channels. In terms of the lateral dimensions (height and width), the kernel is typically much smaller than the image, commonly having a size of 3×3 or 5×5 pixels. The output of the convolution process results in a new array with dimensions of $(H - H_k + 1) \times (W - W_k + 1)$, indicating that the depth dimension is "consumed" during convolution and the lateral dimensions are also reduced. The convolution operation can be visualized as sliding the kernel across the input image, calculating the element-wise product at each position (i, j). The following equation presents the mathematical definition of convolution, as utilized in deep learning:

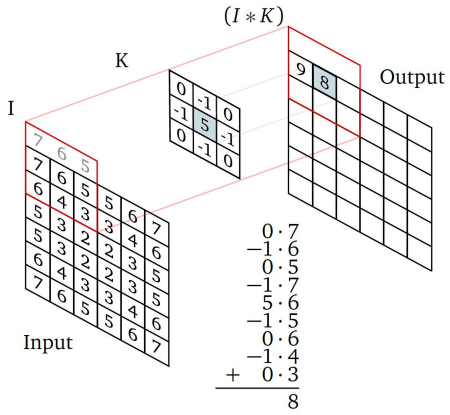

Figure 2.5: An example for the calculation of convolution for a grayscale image [38].

$$(I * K)_{i,j} = \sum_{l=0}^{H_k-1} \sum_{m=0}^{W_k-1} \sum_{n=1}^{C} I_{i+l,j+m,n} K_{l,m,n} \tag{2.3}$$

Where I is the input image, K is the convolution kernel, i, j are the indices of the convolution output array, and l, m, n are the spatial and channel indices. The convolution operation can be reformulated to align with the neuron-equation (2.2), thereby relating each element of the kernel to a weight that is learned by the network through the backpropagation process. Figure 2.5 illustrates an example for the calculation of convolution for a grayscale image. To maintain output with the same lateral dimensions as the input, padding is applied. Padding involves mirroring the border values of the input image with a suitable width.

Within a single convolutional layer, multiple convolutions are performed in parallel on the same input, each utilizing a distinct kernel. As a result, N different two-dimensional images known as feature maps are generated. These feature maps are then stacked together to create the output of the convolutional layer, resulting in a new dimension of $(H - H_k + 1, W - W_k + 1, N)$. Typically, an activation function follows the convolutional layer to introduce non-linearity, and pooling is applied to reduce the lateral extent of the feature maps. The specific details of these operations will be explained subsequently.

Padding, stride, and dilation are techniques used to control the output size of a convolution operation and how it extracts information from the input. Padding in-

volves adding extra values around the borders of an image or feature map. This can be achieved by either using a constant value (typically zero) or reflecting the image border, as demonstrated in Figure 2.5. The width of the padding, denoted as p, determines the extent of the output after the convolution. By applying padding, the lateral size of a feature map can be preserved during the convolution operation. The kernel in a convolutional operation can be moved across the input with a specific step width called the stride. A larger stride (s) leads to a smaller output image, where a stride of two, for example, reduces the output size by half.
The concept of dilation involves inserting zeros into either the kernel or the convolution input. When the input is dilated while using a non-dilated kernel, the output size increases compared to a non-dilated input. On the other hand, if a dilated kernel is used, its effective size becomes larger than its non-dilated counterpart, resulting in a smaller output from the convolution. Dilation allows for the incorporation of long-range correlations into the feature map, as each pixel in the output receives information from a larger area.
A comprehensive and detailed explanation of convolution arithmetic, covering aspects such as padding, stride, dilation, and transposed convolutions, can be found in [39].

Activation Function

Neural networks offer a variety of activation functions [40], all of which share a crucial characteristic: they are nonlinear functions. In contrast, the convolution operation employed in neural networks is linear. Consequently, when multiple convolutions are applied sequentially to generate an output, there exists a single convolution operation that can yield the same output. This implies that a neural network lacking non-linearities would be limited to performing linear regression tasks exclusively. Hence, non-linearities are essential components in enabling neural networks to tackle complex problems beyond linear regression.

ReLU activation
The rectifying linear unit (ReLU) activation function, originally introduced in 1975 [41] to model the behavior of biological neurons, captures the firing mechanism

of neurons. In biological neurons, firing occurs when the accumulated input surpasses a specific threshold, while the neuron remains inactive otherwise [42]. The ReLU function emulates this behavior by setting all negative inputs to zero and allowing positive inputs to pass through without modification, effectively setting the threshold at zero. This activation function has demonstrated its effectiveness in training neural networks efficiently [43]. The derivative of the ReLU function corresponds to the Heaviside or step function.

$$\text{ReLu}(x) = max(0,x) \tag{2.4}$$

Sigmoid activation

The sigmoid activation function, also known as the logistic function, is a commonly employed activation function distinguished by its distinctive "S" shape. It possesses continuous derivatives and is constrained within the range of 0 and 1. This property makes it suitable for mapping arbitrary values onto this interval. The sigmoid function is often utilized as the final activation in binary classification tasks due to its bounded output range. However, it is not suitable for categorical classification. One advantage of the sigmoid function is its ease of computation for calculating its first derivative.

$$S(x) = \frac{1}{1+e^{-x}} \tag{2.5}$$

$$S'(x) = S(x)(1-S(x)) \tag{2.6}$$

Pooling

Pooling is a technique utilized to decrease the dimensionality of data, thereby reducing the amount of information transmitted through the network. Various types of pooling exist, with the most common one being max pooling. In max pooling, an input array is divided into blocks of size $n \times n$, and each block is replaced with its maximum value. Alternatively, other pooling variants calculate the average value within each block. Pooling operates independently on each depth layer, modifying only the lateral dimensions. For instance, using a 2×2 max pooling size discards 75% of the input information, effectively reducing the number of pa-

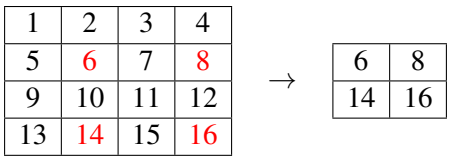

Figure 2.6: Example of max pooling with a 4x4 input array and 2x2 pooling

rameters in subsequent layers. This reduction mitigates the risk of overfitting and accelerates computation speed.

Loss Function

The loss function evaluates the deviation between a prediction and the true values, serving as a crucial factor in the training success of a network. The choice of the loss function depends on the specific task at hand, and there can be multiple suitable options. Determining the appropriate loss function relies on empirical analysis and consideration of the task's characteristics. For instance, if the neural network aims to approximate a function, such as in regression tasks, the mean squared error (MSE) is a suitable choice. However, for classification tasks where the dependent variables are discrete (0 or 1), other loss functions are more appropriate since they accommodate the nature of classification. Classifications are typically represented as vectors, where the dimensionality of the vector corresponds to the number of classes, denoted as C. Each entry in the vector represents a specific class. When constructing a ground truth vector to represent class i, the i^{th} entry is assigned a value of one, while all other entries are set to zero. On the other hand, the network output is obtained through functions, which produce real-valued entries that are normalized to sum up to one. This network output can be interpreted as a probability distribution. The discrepancy between the true probability distribution and the predicted distribution is commonly assessed using metrics such as binary/categorical cross-entropy [40].

$$H(y_t, y_p) = -\sum_{i=1}^{C} \mu_i y_{t,i} \log(y_{p,i}) \tag{2.7}$$

Where H represents the cross-entropy loss function, y_t represents the ground truth vector, y_p is the predicted probability distribution vector, C is the number of classes, and μ_i represents the weight or importance assigned to class i.

In a classification task where classes are mutually exclusive, the true probability distribution only assigns a value of one to a single class. The categorical/binary cross-entropy loss function takes this into account by disregarding predictions for all other classes and placing logarithmic weight on the prediction for the true class. As a result, the loss can range from infinity for a completely incorrect prediction to zero for a perfectly accurate prediction. In segmentation tasks, the categorical/binary cross-entropy is computed for each pixel in the output probability map and then averaged across all pixels.

2.3 Fuel Type

Different geological conditions result in varied vegetation and tree species. However, it is not feasible to analyze all types of vegetation and trees due to the limited scope of the project. The study will focus mainly on vegetation and tree species in Alberta. Therefore, the primary sources for the study will be reports from either the province or Forestry Canada.

In general, trees with needles (coniferous) burn faster and more intensely than trees with leaves (deciduous) [44]. Nevertheless, there is a slight exception to this general rule. Deciduous trees can become highly flammable in early spring, just before the emergence of new leaves. At this time, the trees have low moisture levels, which increases their susceptibility to fire until the new leaves grow [44]. Coniferous trees are known for containing a high quantity of sap in their branches, which is a highly flammable substance that can accelerate the spread of wildfires. Unlike deciduous trees, conifers tend to grow in closer proximity to one another, allowing fires to easily spread from treetop to treetop. In Alberta, coniferous trees such as lodgepole pine, black spruce, white spruce, and balsam fir are widespread and can burn up to ten times faster than leafy trees due to the combustible nature of their sap.

One may wonder why leafy trees burn at a slower rate. The behavior of fire differs

based on the type of vegetation present. Deciduous forests usually function as natural fuel breaks, as they slow down the spread of fire. In the boreal forest, crown fires often stop when they enter an aspen stand. The fire's ability to spread depends on the understory plants and shrubs' amount and type. Due to the lack of ladder fuels in deciduous forests, fire does not usually reach the high crowns of these trees. Aspen's physical characteristics also help resist intense fire behavior, including high crown base height, high moisture content in the leaves and stems, and tight, smooth bark. In coniferous forests, the rough, loose bark can act as a ladder, allowing fire to climb into the canopy, and can also produce embers that spread ahead of the fire front [44]. Alberta has common species such as trembling aspen, balsam poplar, and white birch.

Moreover, in a wildfire situation, structures such as houses can pose a significant threat by adding to the overall fuel load. If these structures are ignited, it can create a domino effect, with the fire spreading to the surrounding vegetation and rapidly intensifying in strength. The situation can be particularly dangerous in suburban and urban areas where buildings are often situated close together, making it easier for fires to spread from one structure to another. The merging of multiple fires can result in a firestorm, which is an extreme and life-threatening event that is very difficult to contain. Firefighters may face challenges in protecting human life and property once a firestorm has taken hold. Therefore, it is important to take proactive measures to reduce the risk of structure ignition in high-risk areas. This can be done through various methods such as minimizing the presence of flammable materials around structures and using fire-resistant materials when constructing buildings. By taking these precautions, the risk of structures becoming ignition sources can be significantly reduced, ultimately helping to prevent the spread of wildfires and safeguarding human life and property.

2.3.1 National Guide for Wildland-Urban Interface Fires

The National Guide for Wildland-Urban Interface Fires [20], developed by the National Research Council of Canada (NRC), serves as a reference document for assessing hazards and fire exposure, protecting property, enhancing community resilience, and planning emergencies, all to reduce the effects of wildland-urban

Table 2.1: Wildland Fuel Types

Fuel Type	Description
F0	Non-vegetated land Cultivated or irrigated landscapes
F1	Deciduous forest Mixed coniferous and deciduous forest with $\leq$ 25% conifer Grassland and cereal cropland (FBP Fuel Types: D1, M1 and M2 with $\leq$ 25% conifers, O1, S1, S2, S3)
F2	Mature conifer forest with $\leq$ 20% standing dead trees Mixed coniferous and deciduous forest with $>$ 25% conifers (FBP Fuel Types: C1, C3, C5, C6, C7, M1 and M2 with $>$ 25% conifers
F3	Upland boreal black spruce forest Dense immature jack pine forest Mature conifer forest with $>$ 20% standing dead trees (FBP Fuel Types: C2, C4, M3, M4)

interface fires.

The National Guide for Wildland-Urban Interface Fires provides Table 2.1, detailing four unique types of fuels. These ”F” type fuels correspond to the categories outlined in the Forest Fire Behavior Prediction (FBP) system [45]. For a clearer insight into the fuel categorization as per the FBP system, Figure 2.7 shows a flowchart representing the FBP-based classification of forest fuels, particularly focusing on those prevalent in Alberta. For an in-depth description of these fuel types, refer to the appendix F of the National Guide for Wildland-Urban Interface Fires [20].

2.4 Topography Analysis

The fire behavior triangle is composed of three main parameters, namely topography, fuel, and weather. Topography, along with fuel and weather, plays a significant role in determining how a fire will behave [20]. In general, fires spread more rapidly up slopes compared to flat ground due to a number of factors. For instance, slopes bring the upslope fuels closer to the flames, which results in shorter

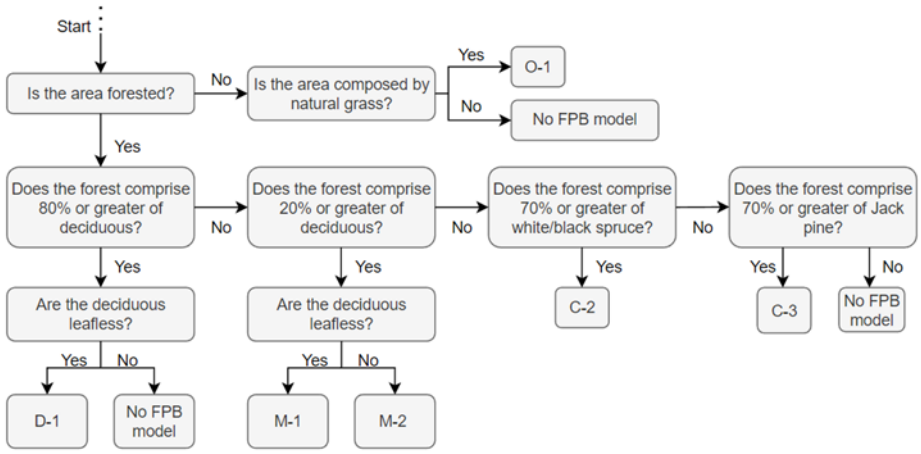

Figure 2.7: FBP classification flowchart from the composition of areas in Alberta, Canada [46]

distances for energy transfer between the flames and fuels. Moreover, the ”view factor” of fuels, in terms of receiving radiant energy that can preheat them ahead of the flames, is improved by slopes. In the FBP System [45], a 70% slope is estimated to cause a spread rate ten times faster than an identical fuel on flat ground under calm wind conditions.

Topography plays a significant role in determining the behavior of fires, as it can influence not only the distribution of fuel and weather but also the flow of wind and the exposure of slopes to solar radiation. For example, narrow canyons can lead to localized increases in wind speed, while the aspect or orientation of a slope can affect its solar radiation exposure. These factors, in turn, can affect the microclimate within fuel complexes and alter key elements of fire behavior, such as fuel moisture and vegetation composition [20]. Therefore, it is important to consider the topographical features of an area when assessing the potential for wildfires and planning mitigation strategies.

According to the National Guide for Wildland-Urban Interface Fires, it is important to manage fuel in specific zones around structures known as Priority Zones. These Priority Zones are defined by a certain radius around the structure and are based on the FireSmart zone concept [47]. The FireSmart program in Canada is a national initiative aimed at reducing the risk of wildfire to buildings and communi-

ties. It involves a multi-faceted approach that includes public education, community planning, development and enforcement of building and land-use policies, and various on-the-ground measures. Central to FireSmart's approach is the identification and management of priority zones around structures. The program typically employs a range of tools for fire exposure assessment, including field surveys, historical fire data analysis, and manual inspections, to identify vulnerable areas and recommend protective measures. While FireSmart's traditional tools rely more on manual assessments and local knowledge, the approach in this study harnesses the power of technology to offer a more data-driven and faster assessment. This can potentially lead to more precise identification of high-risk areas in a relatively shorter time. Figure 2.8 illustrates the Structure Ignition Zone, which comprises Priority Zones 1 to 3. In the guideline [20], another ignition zone, 1A, is defined expanding from 0 to 1.5 meters from a building. This area is highly susceptible to immediate fire threats, as it is the first line of defense against the spread of fire to the structure. Keeping it clear of combustible materials minimizes the risk from embers and radiant heat, effectively creating a protective buffer. However, the detection of fuels from satellite images within this small area near the border of building edges is challenging and requires very high-resolution images. In addition, since ignition zone 1 takes this area into its buffer zone and the building is longer in one dimension [20], the study focuses on priority zones 1 to 3. For a more detailed understanding of the specific parameters and characteristics that define each priority zone within the guidelines, I strongly encourage readers to refer to the guidelines themselves.

The impact of land slope on ignition zones can be a crucial factor that should be considered in the Priority Zones specified as follows:

- Adjust the outer radii of Priority Zones 2 and 3 based on the slope of the land.
- If the slope of Priority Zone 2 or 3 is between 30% and 55%, the outer radius of the zone should be increased by (Figure 2.9):
  - a factor of 2 in the downslope direction, and
  - a factor of 1.5 in the horizontal direction.

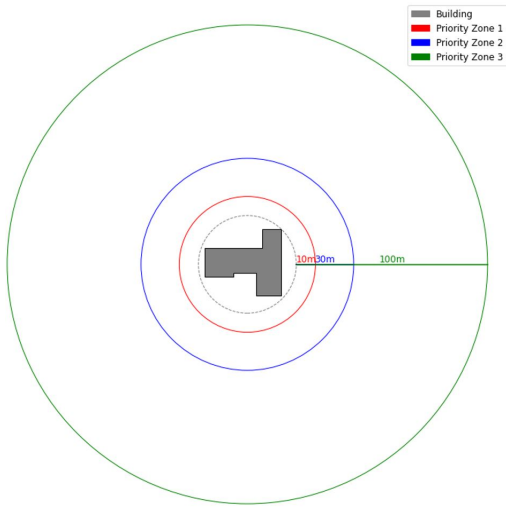

Figure 2.8: Structure ignition zone with priority zones

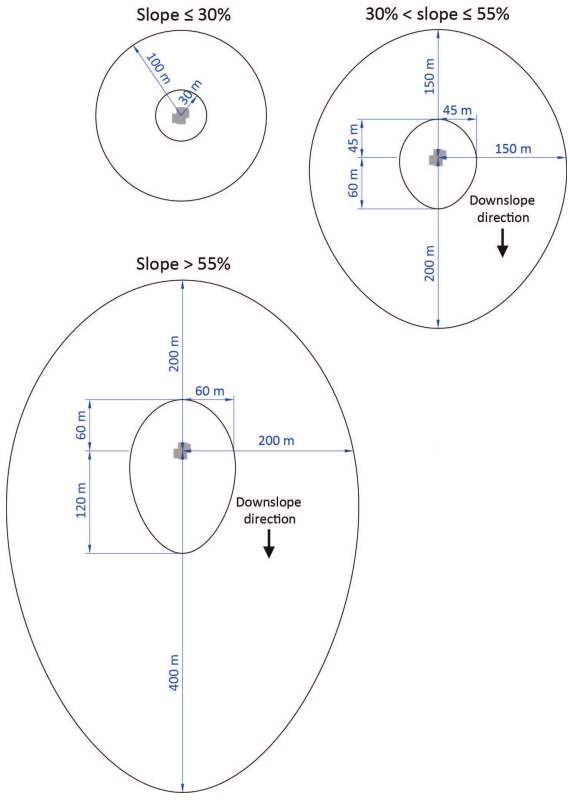

Figure 2.9: Considering of slope for adjustment of Priority Zones 2 and 3 [20]

- If the slope of Priority Zone 2 or 3 exceeds 55%, the outer radius of the zone should be increased by (Figure 2.9):
  - a factor of 4 in the downslope direction, and
  - a factor of 2 in the horizontal direction.

2.5 Fire Exposure Assessment

In wildfire management, understanding the distinctions between fire exposure assessment, fire hazard assessment, and fire risk assessment is crucial. Fire exposure assessment predominantly focuses on evaluating the potential radiant heat and ember fire impacts on structures. This assessment evaluates the potential for structures or areas to be impacted by heat of fire and falling embers, taking into account factors such as proximity to fire sources and the surrounding environment. Fire hazard assessment, on the other hand, delves into the likelihood of an area to ignite and sustain a fire, considering the environmental and physical characteristics such as fuel availability, moisture content, and terrain. Lastly, fire risk assessment offers a comprehensive view, intertwining the probability of fire occurrence (hazard) with its potential consequences (exposure), thereby assessing potential damage to life, property, and ecological resources. As the focus of the study is mainly on fire exposure assessment, I will employ guidance on exposure factors, helping to create a map for the fire exposure assessment of the city of Edmonton.

Wildfires can cause significant damage to buildings through three primary modes of transfer. The first mode is convection, which involves the heating of air surrounding the fire, potentially spreading the flames to nearby structures. The second is ember transfer, a process where burning materials are lofted and carried by the fire's buoyant upward flow up to a 4-kilometer travel distance, resulting in what is often referred to as "ember rain." This can transport embers hundreds of meters downwind, with the density of these embers decreasing as the distance from the fire source increases. The third mode is heat radiation, where heat radiates from the fire source. This radiative heat transfer is influenced by both time and distance, meaning that factors like weather have a less direct impact on it [20]. While the intensity of radiant heat can be high, its peak duration is typically short, decreas-

ing rapidly with distance from the fire, making it particularly critical for objects within 100 meters of the fire source [20]. Wildland fires typically spread with a continuous flame front, driven by wind direction, which preheats vegetation ahead of the fire through radiation and facilitates the spread by lofting embers that can ignite new fires. Figure 2.10 shows a simple visualization of ember and radiation fire transfer.

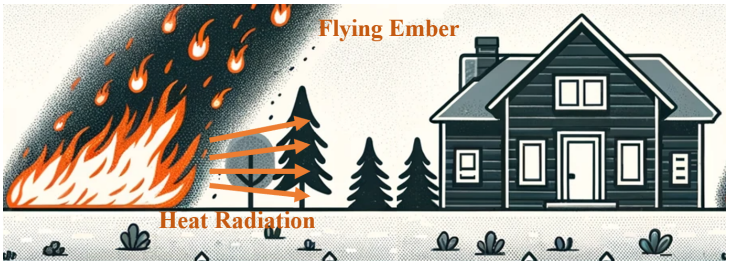

Figure 2.10: Visualization of wildfire transfer from ember and radiation. Image generated by DALL·E, OpenAI, 2024

Although wind-driven embers pose the most significant risk to residential properties during wildfires, this study focuses on heat radiation for its exposure assessment. This approach is primarily driven by two reasons. First, assessing ember exposure necessitates detecting fuels over a larger area (up to 4 km), including various types like wooden sticks and leaf litter, a task that is difficult to accomplish using satellite imagery. Second, the dynamics of ember transfer are greatly influenced by changing weather conditions, including wind speed and direction. Given that such factors demand a constantly updating, dynamic system to reflect real-time conditions, incorporating this data into the study would necessitate a sophisticated computational framework and real-time data integration, which adds complexity to the analysis.

When Figure 2.12 shows a Hazard Level greater than 1, an exposure assessment needs to be conducted to determine the risk of wildfire to a location. This assessment considers factors like the type and amount of fuel present and the topography. Therefore, in accordance with the guidelines provided in [20], table 2.2 has been compiled to assist in performing an exposure assessment that focuses on heat radiation transfer within the priority zones, as illustrated in Figure 2.8.

Table 2.2: Exposure from fuels in priority zones (0-100 m from the structure)

Distance from structure, m	Surface fuel	Fuel type	Exposure
0-10	Green lawn, non-woody plant, or non-vegetated	-	Nil
	Continuous plant litter, dry grass, bark mulch	-	Moderate
	Hazard shrubs or trees	-	High
10-30	Green lawn or vegetation	Deciduous or no tree (F0, F1)	Nil
		$\leq 25\%$ conifer tree cover (F2, F3)	Moderate
		$> 25\%$ conifer tree cover (F2, F3)	High
	Continuous plant litter or dry grass	Deciduous or no tree (F0, F1)	Low
		$\leq 25\%$ conifer tree cover (F2, F3)	High
		$> 25\%$ conifer tree cover (F2, F3)	High
30-100	-	F0	Nil
		F1 (Fuel cover $< 10\%$)	Low
		F1 (Fuel cover $10-50\%$)	Moderate
		F1 (Fuel cover $> 50\%$)	High
		F2 (Fuel cover $< 10\%$)	Moderate
		F2 (Fuel cover $10-50\%$)	High
		F2 (Fuel cover $> 50\%$)	High
		F3 (Fuel cover $> 5\%$)	High

2.5.1 Building Resilience: Strategies Against Wildfires

In the context of increasing wildfire risks, particularly in regions prone to such natural disasters, the resilience of residential and commercial structures against fire becomes a matter of paramount importance. The focus on enhancing a building's resistance to wildfires typically centers around its structural design and the materials used in its construction. In the following, I will explore a range of strategies and best practices from guidelines [20, 48] for constructing and maintaining buildings in a manner that reduces their vulnerability to wildfires.

- **Exterior walls:** Using fire-resistant materials for exterior walls is crucial. Materials with a high fire-resistance rating, such as non-combustible siding or treated wood, can significantly reduce the vulnerability of the structure.

Ensuring that all joints in the external wall cladding are covered and sealed, leaving no unprotected gaps larger than 3 mm, further prevents the ingress of embers.

- **Foundation walls:** Constructing foundation walls from insulating concrete forms or unit masonry not only provides structural stability but also adds a layer of fire resistance. This helps in preventing the spread of fire from the ground level upwards.
- **Roofing materials:** The choice of materials for the roof, including components like pipes, flashing, roof curbs, and tiles, should be non-combustible. This choice is vital as the roof is often the first part of a building exposed to flying embers.
- **Windows and doors:** Windows should ideally be dual-paned with one pane of tempered glass to withstand heat. Doors should be solid and made from non-combustible or fire-resistant materials to prevent easy penetration by fire.
- **Vents and openings:** Any vents in the building should be covered with metal mesh to prevent embers from entering. Sealing gaps in the building's envelope, especially in areas like wood decking, is crucial to prevent embers from igniting materials inside or underneath the structure.
- **Roof design**: The roof's design should minimize area where debris can accumulate, such as valleys or flat surfaces. As shown in Figure 2.11, the right building roofing design is more fire-resistant.
- **Fire breaks:** Creating natural or artificial fire breaks, such as gravel pathways or concrete barriers, can help prevent the spread of fire to the building.

Developing such a tool that can create a map for assessing the heat exposure level in the case of fire for any individual building by detecting fuel types using machine learning techniques, in accordance with guideline notes has potential applications and users across various sectors. To address the question of "Who" can use this method and "How", the following options can be considered:

- **Urban planners:** The proposed method can be valuable in designing fire-

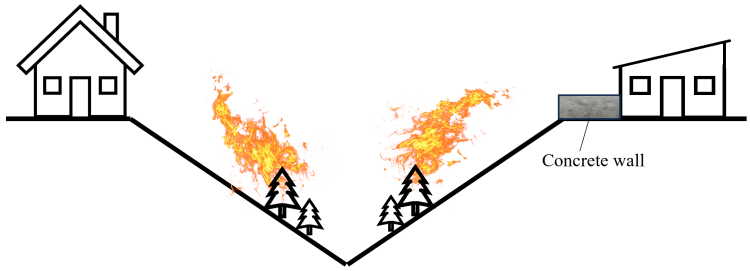

Figure 2.11: Structural design for fire safety in uphill

resilient communities. They can make informed decisions on building materials, construction methods, and community layouts to mitigate a portion of fire hazards.

- **Fire departments:** The agency can utilize the proposed methodology for pre-incident planning and risk assessment. The ability to map potential heat radiation exposure can aid in developing more effective firefighting strategies and evacuation plans.
- **Environmental and forestry agencies:** These organizations can use the method for managing forested areas near urban developments. By analyzing fuel types and potential fire behavior, they can implement targeted fire prevention measures, such as controlled burns or vegetation management.
- **Homeowners and community associations:** They can use the method to assess the risk to their properties and take proactive steps to reduce fire hazards. This could include modifications to landscaping and building materials.

! To facilitate the application of this method, the creation of an intuitive software tool that integrates this methodology could broaden its accessibility, making it more user-friendly for a diverse array of users such as homeowners.

2.6 Study Area

2.6.1 Statistics of Fire Across Canada and Alberta

Canada, with its unique geographical and climatic conditions, is one of the countries that face significant challenges with wildfires. With an increasing population, expanding cities, and growing infrastructure, the issue of wildfires has become even more pressing. In this section, I will delve into the statistics of fires that have occurred in Canada, with a particular focus on the province of Alberta. To gather the data, I relied on the National Forestry Database of Canada [49], which provides a comprehensive picture of the wildfire situation across the country.

The hazard level of wildfires in a given area is a critical aspect that requires close attention. The image presented in Figure 2.12 depicts a historical wildfire hazard map that is based on spatial burn probability outputs obtained through simulations of wildfire growth using historical weather and wildfire location data. The map was generated by analyzing 30 years of fire history data. In the map, areas are classified according to four hazard levels, with a rating of 1 indicating no further action is required [20]. In addition to that, the data presented in Figure 2.13 shows the incidence of wildfires across Canada spanning from 1990 to 2021. The visual representation indicates a gradual decline in the frequency of wildfires as time progresses. This trend may be attributed to the implementation of preventative measures as well as the increase in public awareness about wildfire safety. Nonetheless, it is important to note that despite the decreasing trend, it is still critical to remain vigilant in protecting ourselves from the danger of wildfires. We must not become complacent in our efforts to prevent and manage wildfires and instead continue to take all necessary precautions to safeguard our communities from this natural hazard. By doing so, we can ensure the safety and well-being of ourselves and our surroundings, and minimize the potential damage caused by these catastrophic events.

Figure 2.14 shows the total area of land that was burned by wildfires in Canada between 1990 and 2020. The data reveals that approximately 746,000 km^2 of land were affected/burned by wildfires during this period, which equates to approximately 7.5% of Canada's total land area. This statistic is particularly alarming and

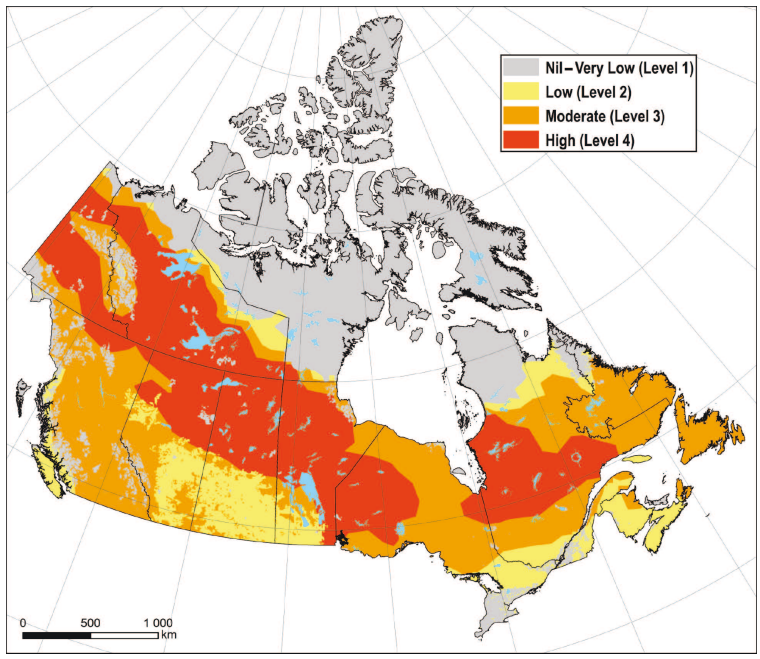

Figure 2.12: historical wildfire hazard map. Generate from a 30-year fire history [20]

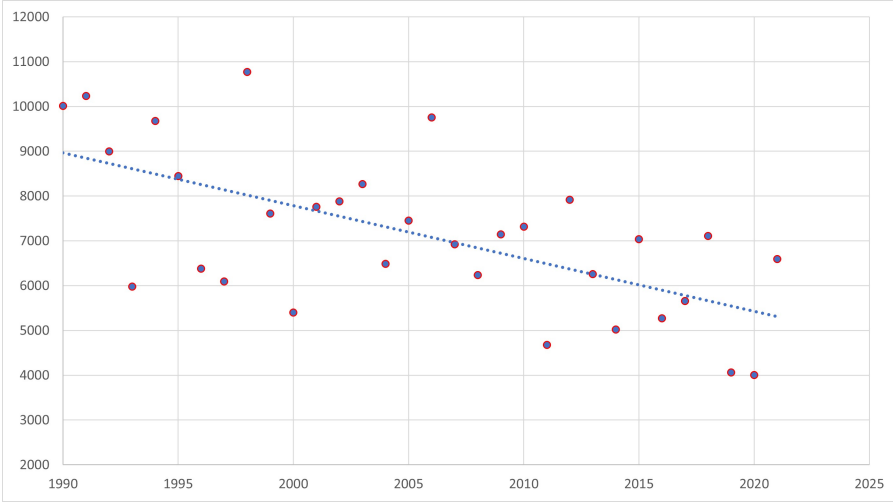

Figure 2.13: Number of fires across Canada between 1990 to 2021 [49]

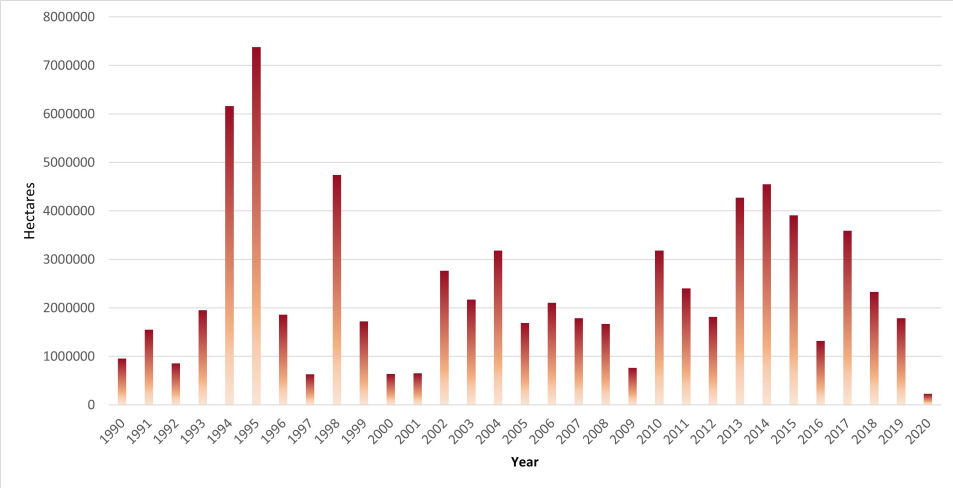

Figure 2.14: Burned area in Canada as a result of wildfire between the year 1990 to 2020 [49]

highlights the significant impact that wildfires can have on the environment and communities in Canada. Canada experienced 302,905 wildfires from 1981 to 2018, out of which 0.2% (685 fires) necessitated the evacuation of roughly 400,000 individuals. Furthermore, a total of 96 of these incidents resulted in the loss of buildings, including residential homes, recreational properties, and businesses, leading to the destruction of approximately 4,015 structures [50].

The chart in Figure 2.15 illustrates the incidence of fires across various provinces in Canada in the year 2020. It is evident that the majority of the fires occurred in Alberta, with Quebec and British Columbia following closely. Therefore, it can be inferred that Alberta requires significant and effective preventive measures to mitigate the occurrence and spread of fires. This information could prove useful in developing targeted strategies and allocating resources to areas most susceptible to fires.

The chart depicted in Figure 2.16 shows the count of fire incidents that occurred on a monthly basis in the province of Alberta, covering the period from 1990 to 2019. The graph offers a visual representation of the frequency of fires during each month in the mentioned period, highlighting any potential seasonal patterns or trends. It is evident that the period of middle spring and early summer experiences the most

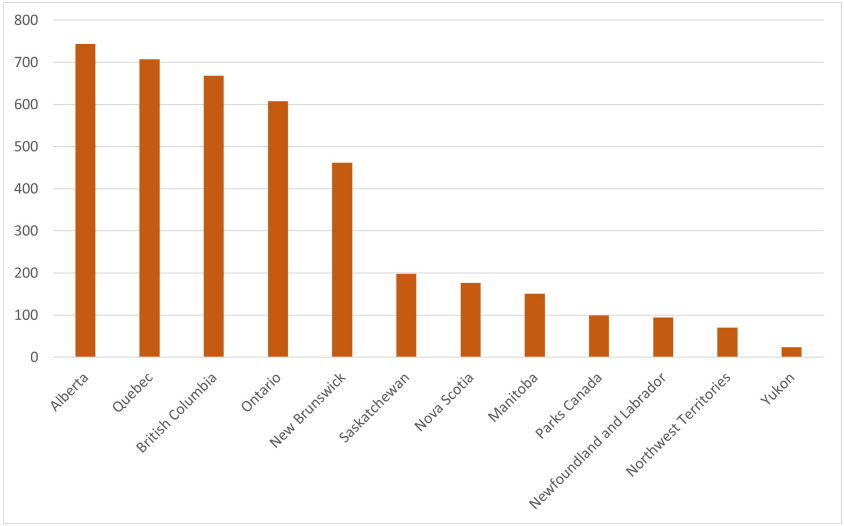

Figure 2.15: Number of fires by province in Canada in the year 2020 [49]

significant frequency of fires.

2.6.2 Study Area Overview

To obtain a broad understanding of the distribution of green vegetation across the city of Edmonton, I conducted an analysis using the NDVI. This analysis facilitated the assessment of vegetation presence and density throughout the city, offering valuable insights into the overall green landscape. To gather the satellite imagery required for conducting NDVI analysis, I initiated the process by accessing the Landsat 8 satellite images with TIF format (Tagged Image File Format) consisting of 11 distinct bands through the USGS global visualization viewer [51]. To ensure that the imagery provided a comprehensive representation of green vegetation, I implemented a careful selection process that restricted the cloud cover to a range of 0 to 20%. Furthermore, I specifically opted for satellite images captured during June, taking advantage of the favorable environmental conditions during that time. The reason behind choosing a summer satellite image for NDVI analysis is as follows: during summer, vegetation is typically at its peak, resulting in higher NDVI values indicative of dense, healthy greenery. Conversely, in winter, vegetation may be obscured by snow, leading to lower or even negative NDVI values. The

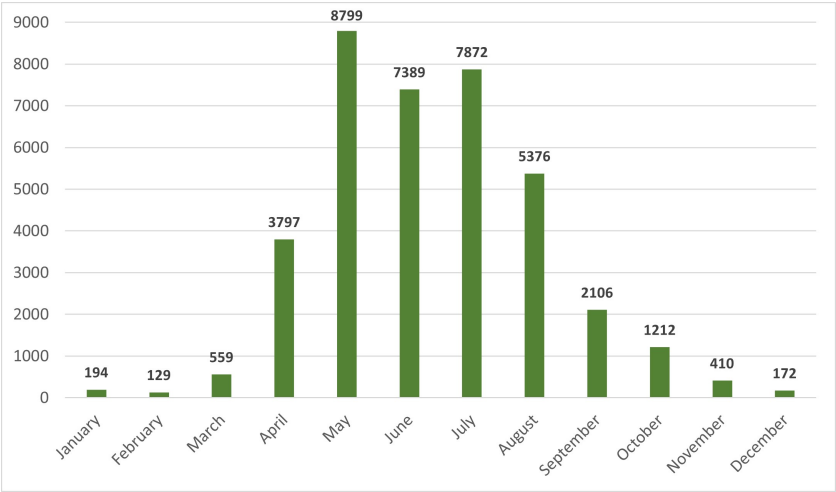

Figure 2.16: Number of fires by month in the province of Alberta [49]

presence of snow and ice, which reflect visible light while absorbing near-infrared light, further impacts NDVI readings. Seasonal atmospheric conditions, such as varying levels of cloud cover, humidity, and particulate matter, also affect the light reflection and absorption, thereby influencing the imagery. Additionally, the sun's angle changes with the seasons, altering landscape illumination and potentially creating more shadows in winter, which can impact NDVI calculations.

Figure 2.17 shows the NDVI values using a color ramp from red to green. In this representation, green indicates healthy vegetation (with a maximum value of 1), various shades of yellow represent areas with limited or no vegetation, and moving towards red signifies regions devoid of any vegetation (with a minimum value of -1). The findings presented here demonstrate that water and developed areas exhibit very low NDVI values (depicted as dark shades). This suggests that these land covers reflect more light in the visible band than in the near-infrared. In contrast, the urban build-up areas display low to moderate NDVI values, represented by various shades ranging from light green to orange. On the other hand, more densely vegetated regions show moderate to high NDVI values, presented in varying shades of green. These areas have stronger near-infrared reflectance, indicating healthier vegetation or varying chlorophyll content.

Various studies have proposed NDVI values for different major classes in urban

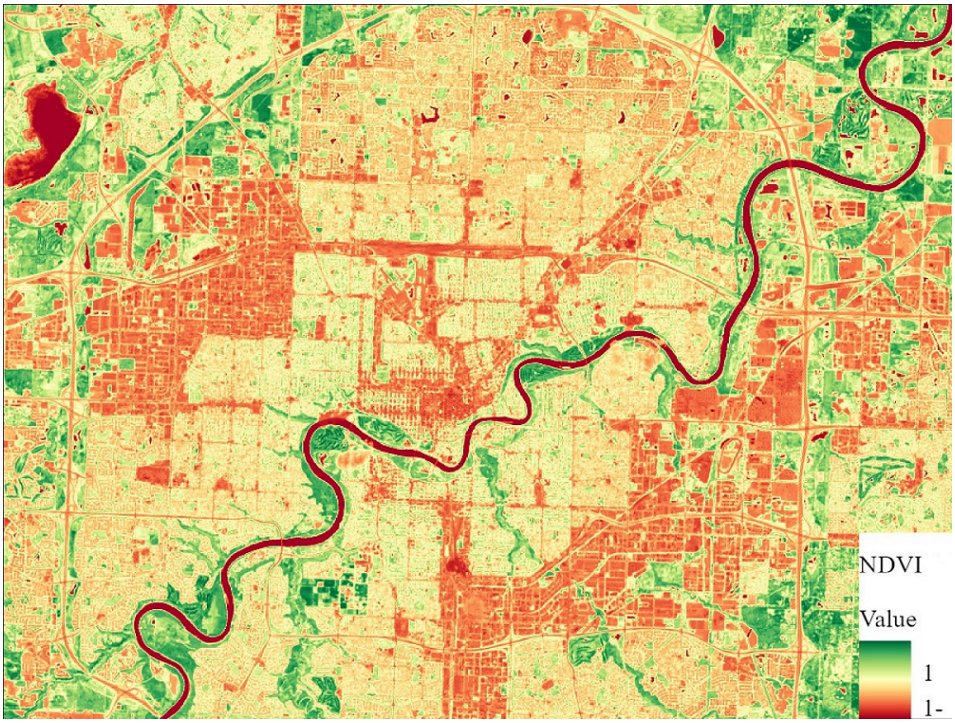

Figure 2.17: NDVI map for the entire city of Edmonton

areas, e.g., [52, 53]. In this study, I adapted the suggested threshold values to accurately identify land cover types based on satellite imagery. The water class falls within the range of -1 to -0.04, build-up and barren areas within -0.04 to 0.25, grassland and sparse vegetation within 0.25 to 0.4, and dense vegetation within 0.4 to 1. The classified NDVI map for the city of Edmonton is shown in Figure 2.18. The obtained result from the analysis provides valuable insights into identifying areas and buildings that are more susceptible to experiencing high fire exposure during a wildfire event. This assessment is made possible by considering both the amount and density of vegetation present in the vicinity of the designated areas or buildings. By utilizing the NDVI data and analyzing the vegetation distribution across the landscape, it becomes feasible to pre-evaluate the potential fire risk associated with different regions.

The Kinsmen Sport Center building holds significance as one of the notable locations identified by the City of Edmonton for assessing and mapping the wildfire

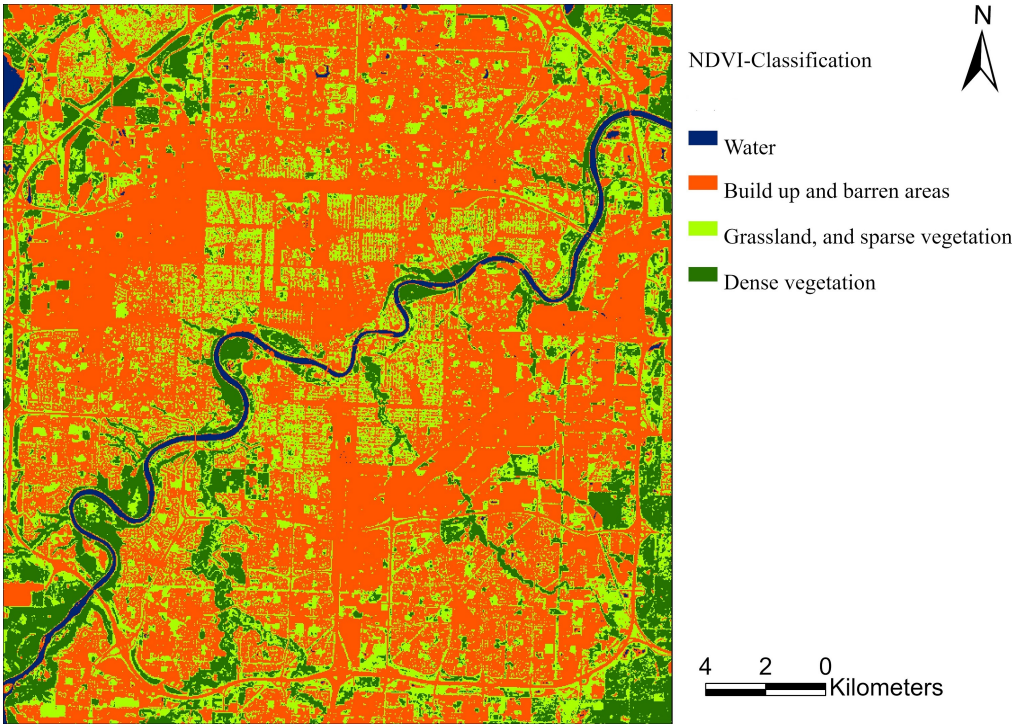

Figure 2.18: Classified NDVI map for the entire city of Edmonton

hazard in its vicinity. Given that the project received funding from the city, the research efforts were primarily directed toward examining this specific building. In addition, the building presents an excellent opportunity for satellite analysis due to its proximity to various fuel types such as deciduous trees, conifer trees, and ground vegetation (grass). These factors render the building susceptible to wildfires. Google's 3D model of the Kinsmen Sport Center and its neighborhood is illustrated in Figure 2.19.

Figure 2.19: Google's 3D model of the Kinsmen Sport Center and neighborhood. Imagery ©Google, Imagery ©2022 Maxar Technologies

2.7 Previous Studies

2.7.1 WUI Wildfire Risk

Research into wildfire risk in the WUI usually involves modeling potential wildfire intensity or exposure using various factors like vegetation, topography, and housing density [12–14]. While these large-scale assessments help with broad spatial comparisons, they have a significant drawback: they cannot accurately predict wildfire risk at the level of individual buildings or neighborhoods. This limitation arises because the threat to structures from wildfires is heavily influenced by local factors rather than broader landscape characteristics [15]. Both modeling and experimental investigations have demonstrated that the potential for structure ignition by wildfires is significantly influenced by a specific portion of the WUI situated within 30-100 meters of buildings. This critical area is commonly referred to as the Home Ignition Zone [8, 16, 17]. The likelihood of ignition primarily depends on how wildfires behave within the HIZ, which depends on factors such as fuel types and slope [18, 19]. These insights have been incorporated into guidelines for mitigating ignition hazards by organizations like the National Research Council Canada [20].

Despite the critical role of local factors in wildfire risk, only a few numbers of spatially detailed studies focus on the HIZ. Gibbons et al. [54] conducted research on an Australian wildfire measured variables such as the coverage of trees/shrubs within 40 m, the upwind distance from homes to vegetation, and the count of buildings within 40 m of buildings. Research conducted in southern California [55] and Alberta, Canada [56], assessed the spatial morphology of buildings and their connection to ignition risks. A study on the Hayman Fire in Colorado assessed elements like terrain slope, distance to a fire station, density of vegetation, and the extent of defensible area around buildings [57]. The utilization of Light Detection and Ranging (LIDAR) to characterize the pre-fire land cover and topographical analysis within HIZ [58]. Such studies emphasize local scales such as individual buildings and local communities, generally using parameters related to land conditions (usually limited to the percentage of vegetation cover) and topography (typically limited to slope). Nevertheless, these studies often require extensive manual creation of a dataset and analysis, which can be time-consuming, especially for assessments of large-scale areas.

2.7.2 Aerial-Based Remote Sensing

Detecting individual trees and determining their location and species is a difficult task that necessitates high-resolution aerial-based images and, if feasible, height information collected by LIDAR. This section delves into recent effective techniques that have demonstrated promising outcomes in the realm of vegetation remote sensing, along with a few previous studies pertaining to the topic.

Different machine learning techniques have been used in a new era in the field of aerial-based vegetation mapping. These advanced computational methods have enhanced the precision and efficiency with which I can analyze and interpret aerial images to map vegetation cover. Supervised classification techniques, as a subcategory of machine learning, are frequently utilized to create vegetation maps using aerial-based images. For example, Réjichi and Chaâbane [59] used the support vector machine (SVM) method to generate spatial-temporal vegetation maps, while Wei et al. [60] utilized the decision tree algorithm to map vegetation cover. Zhang and Xie [61] used an artificial neural network (ANN) to produce a vege-

tation map from Airborne Visible/Infrared Imaging Spectrometer (AVIRIS) data, while an SVM approach was used by Tigges et al. [62] to classify urban vegetation from various temporal and spectral band mixtures of five RapidEye images for Berlin, Germany. To classify urban vegetation characteristics from QuickBird satellite images for Vancouver City, Canada, Tooke et al. [22] employed spectral unmixing and a decision tree approach. On the other hand, unsupervised classification algorithms such as the Iterative Self-Organizing Data Analysis (IOSDATA) technique [63] and K-Means [64] method have been commonly used for vegetation cover classification from aerial imagery [65]. Deep neural networks (DNNs), a type of ANN, are increasingly used in remote sensing applications as they are able to detect features in multiple levels of representation [24]. The popularity of these techniques stems from their ability to encode both spectral and spatial information directly from raw images without the need for preprocessing[66]. Xie et al. [67] utilized CNN to differentiate between tree species in urban areas based on a single-band image called the Canopy Height Model (CHM). CHM, which is captured from a satellite view, represents the height of various objects such as buildings and trees through pixel values rather than colors.

The majority of tree species identification tools have primarily concentrated on forest regions, with very few investigations assessing the effectiveness of high-resolution imagery for identifying urban tree species. In contrast to forested regions where trees are often closely spaced and the surrounding terrain is relatively uniform, urban areas have diverse and complex land cover, which poses particular difficulties for tree species classification. Urban areas face the challenge of shadows caused by tall buildings that obscure or entirely block spectral data from shaded tree species, making them difficult to classify or interpret. The classification of densely packed trees in urban regions poses a significant challenge due to the presence of multiple tree categories and the difficulty in detecting individual tree canopies [68, 69].

Zhang et al. [70] put forth a collection of RGB optical images obtained by UAV which included ten urban tree species. The aim was to investigate whether deep learning models such as AlexNet, VGG-16, and ResNet-50 could be employed for the classification of individual tree species. They reported that ResNet-50 had a higher accuracy of 92.6% for tree species classification compared to AlexNet

and VGG-16. The model was trained using approximately 80% of 30,000 images. However, the accuracy was lower for tree canopy images with complex backgrounds than those with simple backgrounds. Furthermore, the classification accuracy of ResNet-50 for deciduous tree species was higher in summer than in autumn.

Abdollahi and Pradhan [71] implemented a DNN model in vegetation mapping from high-resolution remotely sensed imagery. For classification purposes, they chose three images from the Aerial Imagery for Roof Segmentation (AIRS) dataset [72], which had a spatial resolution of 7.5 cm and dimensions of 2500×3000. Because the images used were RGB, they decided to use the HSV (hue, saturation, and value) color space of the images instead of RGB. Using the HSV color space helps distinguish between color and illumination and reduces the impact of illumination variations on the color of the object. An explanation model called Sharpley additive explanations (SHAP) was utilized for interpreting the output of the DNN model [73, 74]. Based on their results, authors achieved a classification of vegetation into two groups - High-Vegetation and Low-Vegetation. Their method was able to attain an accuracy rate of 92.66% for the F1 score [1]. While the model was successful in accurately identifying vegetation, it was not able to differentiate between different categories of vegetation.

Pu et al. [75] conducted a study in which they compared the effectiveness of IKONOS and WorldView2 satellites for classifying seven types of trees in Tampa, Florida, USA. They first classified the vegetation by using a threshold value of 0.25. The findings indicated that WorldView2 data achieved a higher overall classification accuracy of approximately 55% than IKONOS. However, the results also revealed that even with the information provided by the WorldView2-8 Band data[2] (which provide way more information than 3-band RGB data), the accuracy of identifying and mapping all seven tree species/groups was still relatively low and did not meet the general requirement for most applications.

The studies mentioned below focused on identifying individual palm trees. Srestasathiern and Rakwati [76] carried out their research in Thailand using Quickbird and WorldView-2 images with four spectral bands and 60 cm spatial resolution. They used a data

[1] A measure used in machine learning for evaluating the accuracy of binary classifications.

[2] 8 multispectral bands includes: coastal blue, blue, green, yellow, red, red edge, NIR1, and NIR2

transform and maximum extraction to determine the palm positions based on a vegetation index, achieving an F1-Score ranging from 89.7% to 99.3%. It is worth noting, however, that their algorithm was tested on plantations where the individual palm trees were distinct and there were no overlapping crowns, and where the plantation boundaries were already delineated.

Li et al. [77] conducted a study on classifying urban trees in WorldView-3 images at a 30 cm resolution. They segmented the images into super-pixels using a region-growing algorithm and then extracted various features such as mean, variance, and spectral indices for each polygon. An SVM classifier was employed for classification. The authors achieved an accuracy rate of 80% - 92% for five different species; however, they were unable to detect the individual trees or classify them by species.

Rezaee et al. [78] utilized satellite imagery from the same source to classify trees in Canada. They followed the same image segmentation approach as Li et al. [77], but used a VGG16 CNN to classify the polygons into four species. They obtained their training data from on-ground sources and achieved an accuracy of 82% overall. However, the authors did not provide sufficient information about their dataset, so the extent of their accomplishments is uncertain. In addition, they used the source images from Worldview-3 satellite which has 8 visible-near infrared bands.

In a study conducted in Finland, Nevalainen et al. [79] obtained an extensive on-ground validated set of 4100 reference trees. They used a UAV to capture hyperspectral data of the study area with a high resolution of 5 cm and 33 bands. Using automatic image matching, they created a three-dimensional digital surface model (DSM) from this data. The watershed transform was then applied to segment individual tree crowns. These segments were classified into four different species using either a multilayer perceptron (MLP) or a Random Forest algorithm, achieving an overall accuracy of 95%. While the results are impressive, the process involved complex preprocessing to generate the DSM and required significant manual labor for operating the UAV.

2.7.3 Ground-Based Remote Sensing

Remote sensing techniques, such as aerial and satellite imagery, have been widely used for vegetation mapping and monitoring in urban areas. However, it is important to note that these methods may not provide dynamic and up-to-date information about the current condition of plants. This is because satellite images are often not updated frequently enough across a city to capture changes in vegetation health or growth on a regular basis. Therefore, while remote sensing techniques can be an effective tool for the initial mapping and monitoring of urban vegetation, they should be complemented with ground-based surveys and other data sources for a more comprehensive understanding of vegetation dynamics in urban areas. This will provide more accurate and up-to-date information for decision-making and management of urban vegetation.
In reality, many local governments continue to rely on time-consuming manual surveys to gather and maintain records of public trees, while private trees often go undocumented. Even though urban trees play a crucial role, national and municipal tree inventory sources suffer from insufficient detail, inconsistency, and quantity, mainly because of the high expenses involved in tracking and monitoring trees over vast areas and extended periods [80].

Recent literature has highlighted two trends in assessing urban greenery along street networks over large areas at a low cost, which has gained attention and is promoted by a larger number of municipalities [81]. The first trend is the growing availability of low-cost, detailed, and crowd-sourced street-level imagery, which comprises photographs of street scenes taken from the ground [82, 83]. The second trend is the success of CNNs in extracting abstract features and objects in imagery, out-competing other methods [84]. Street-level imagery is being used to estimate the percentage of detected tree canopy cover pixels relative to the total number of pixels in an image, which quantifies the ”perceived urban canopy cover” [85]. Similarly, Li et al. [86] used green pixels in street view scenes to estimate the percentage of vegetation in streets.

The technique of using street-level imagery along with deep learning has been employed to improve the accuracy of tree inventories based on coarse street addresses with accurate geographic coordinates [87]. Laumer et al. [87] utilized this method

and were able to match 38% of over 50,000 identified street trees to their respective street-level addresses. Meanwhile, Wegner et al. [88] developed a workflow that combines the results of Faster Region Convolutional Neural Network (R-CNN) tree detection from Google Street View (GSV) and aerial imagery with data from Google Maps in a probabilistic model to automatically detect and geolocate street trees. They were able to classify eighteen different species among the detected trees by using street-level and aerial imagery.

Wegner et al. [88] developed a system that uses CNN to detect and categorize different tree species in urban areas. Their approach involves utilizing a dataset of around 80,000 trees labeled with species information and geographic locations, combined with a diverse range of images from Google Maps, such as aerial and street view images. By leveraging this information, they were able to detect, classify, and maintain a public inventory of trees with GPS location. The results of their study indicate that aerial and street-view images are the most valuable sources for detecting and classifying trees.

Stubbings et al. [81] aimed to develop an automated, consistent, and scalable approach to estimate the hierarchical area-level score of urban street-level trees using recent advances in Deep Convolutional Neural Networks (DCNN) and multilevel regression modeling. They used over 200,000 street-level images from GSV of Cardiff, UK, to apply semantic image segmentation using the PSPNet [89] to classify image pixels and estimate the percentage of vegetation cover. They opted to utilize the Pyramid Scene Parsing Network (PSPNet) with a Chainer implementation by Tokui et al. [90], utilizing a scene parsing approach. The selection of PSPNet was based on three primary reasons. Firstly, PSPNet is particularly designed to analyze urban scenes, making it an appropriate choice for identifying vegetation in street-level images. Secondly, PSPNet utilizes a unique pyramid parsing architecture that leverages both local and global contextual information within images to classify pixels. This enables objects to be classified in the context of other objects, such as a branch within a tree. Lastly, PSPNet has demonstrated superior performance compared to several other popular deep learning algorithms. The method they employed, PSPNet, exhibited a precision and R^2 value of 82% and 83%, respectively, which surpassed the results obtained by other methods such as Random Forest and green-pixel analysis.

Seiferling et al. [85] developed and tested a new method for rapid quantification and mapping of urban vegetation, specifically trees, using more than 400,000 geo-tagged images from GSV in New York City. Their method aimed to demonstrate the ability to accurately quantify the presence and perceived cover of street-side trees at a high spatial resolution at the city-scale. The approach involved sampling sequential neighboring image scenes of the streetscape, using a trained predictor to segment the amount of tree cover in each image, and modeling the relationship between the tree cover of neighboring viewpoints. They compared the accuracy and utility of their approach to contemporary remote-sensing techniques, such as object-based image analysis of high-resolution LIDAR data and multispectral imagery. The images were collected along city roads with a sampling rate of approximately every 15 meters. The test dataset yielded an r-square value of 0.73 and a root mean square error value of 0.28. According to their findings, the performance of the streetscape tree cover predictor was optimal when the images were aligned parallel to the street direction, meaning that the camera's heading was aligned with the street's heading.

In a recent study, Lumnitz et al. [91] developed a new technique to automatically detect and locate trees along street networks in urban areas. Their approach utilized monocular depth estimation [92] and triangulation (to reduce duplicate observations of individual tree predictions and correct their position) to accurately estimate tree locations from a single image without requiring additional data sources. To extract and mask fuzzy features like trees in the images, they employed deep learning frameworks for instance segmentation using Mask Regional CNN architecture, which involves both object detection and pixel masking. They evaluated their approach using images from GSV and validated their model by comparing its output with on-site tree location measurements in the Metro Vancouver area. Their method was able to accurately detect over 70% of public and private trees that were manually recorded in a ground-truth campaign conducted throughout Metro Vancouver. The most remarkable method in their study is the depth estimation using MonoDepth, which is a readily available fully trained unsupervised deep learning model for depth estimation with an error margin of less than 20% [92]. To estimate depth, the model computes disparities (D) between objects in each panoramic image. Afterwards, disparities are transformed into absolute depth in

meters ($depth = \frac{W_0 \times F}{D}$) through a post-processing step that takes the focal length (F) and baseline of the camera (W_0) used to capture the training images as an input. Lumnitz et al. [91] found the distance from ground-truth to tree predictions for street trees ranged from 0.26 to 13.14 m with a mean of 4.31 m and a standard deviation of 2.76 m.

Chapter 3

Methodology

The upcoming chapter provides a concise overview of the methodology, including the topography analysis, vegetation analysis, and mapping hazard zone.
The initial stage involves gathering the topographic data for the entire city of Edmonton. Subsequently, the elevation data points are identified and integrated into the map. Moving on, the next step entails delineating the ignition zones surrounding buildings in accordance with the National Guide for Wildland-Urban Interface Fires [20] guideline outlined in Section 2.3.1. As discussed in Section 2.6.2, the Kinsmen Sport Center Building is the ideal candidate for satellite analysis because of its close location to diverse fuel sources like deciduous and conifer trees, as well as ground vegetation, such as grass. This proximity makes the building more vulnerable to wildfires. To address this, a fuel detection model utilizing a CNN was employed to classify the aforementioned vegetation types and determine their spatial relationship with the building's position. The final step of the methodology involves quantifying the extent of each fuel type within the designated ignition zones. This information is then utilized to create a hazard map specifically tailored to the Kinsmen Sports Centre. By incorporating the data on fuel types and their distribution, the hazard map provides valuable information regarding the potential risk of a wildfire event and allows for effective mitigation strategies to be developed.
Overall, this chapter serves as a comprehensive guide to the methodology em-

ployed in the study, highlighting the steps involved in extracting topographic information, mapping ignition zones, utilizing a fuel detection model, and generating a hazard map. Through these methods, I aim to enhance the understanding of wildfire risks and contribute to effective wildfire management strategies.

The chapter is classified into five different sections that are listed below:

1. Section 3.1: Overview

---

2. Section 3.2: Topography Analysis

---

3. Section 3.3: Tree and Grass Cover Semantic Segmentation

---

4. Section 3.4: Integration of Topography Analysis and Vegetation Segmentation

3.1 Overview

Figure 3.1 illustrates the comprehensive approach of satellite analysis employed for studying wildland-urban interface fires. The analysis comprises three fundamental steps, each playing a significant role in understanding and assessing fire hazards.

The first step involves topography analysis, where the topographic information of the study area, such as the city of Edmonton, is extracted. This process entails capturing and incorporating elevation data points and coordinates of buildings to accurately represent the slope and buildings' location on a map. The second step focuses on tree detection, aiming to identify and delineate areas with dense or single tree cover. By employing CNN techniques, satellite imagery is analyzed to detect and map the distribution of trees in the study area. This step is crucial as trees play a significant role in fueling wildland fires and understanding their distribution helps in assessing fire risk and potential spread. The third step involves ground vegetation mapping, such as grass, within the study area. This information is vital in assessing the fuel availability and flammability of the landscape.

Through the use of CNNs, satellite imagery is analyzed to classify and map the ground vegetation type. By integrating the outcomes of these three steps, a hazard zone map is created around a specific building, such as the Kinsmen Sports Centre in this context. The hazard zone map takes into account the topographic features, tree distribution, and ground vegetation types within the proximity of the building. This comprehensive approach provides valuable insights into the potential wildfire risks associated with the building, considering factors such as fuel availability and vulnerability.

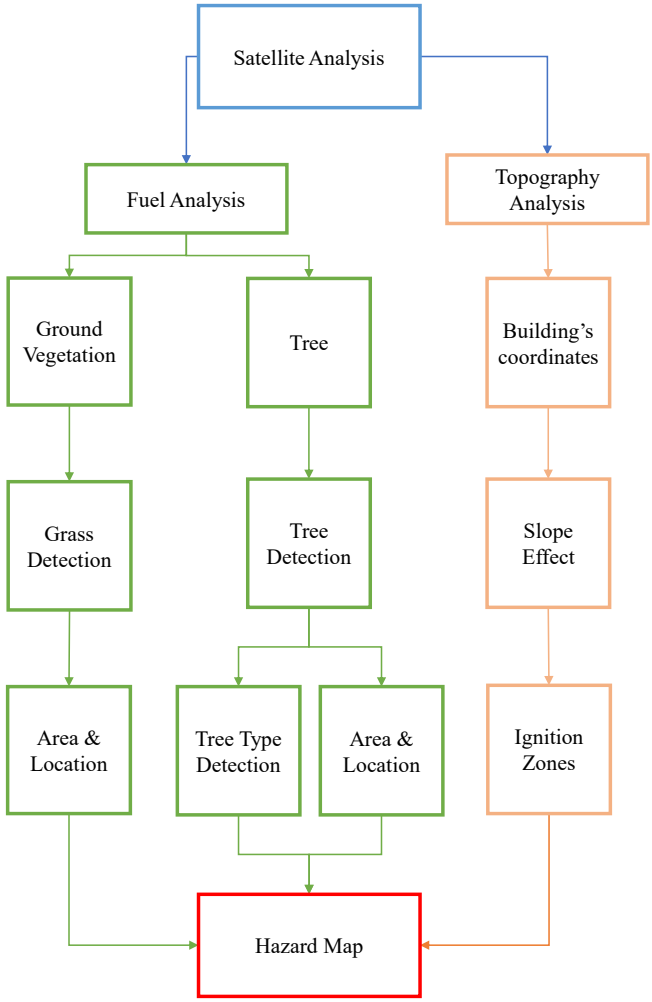

Figure 3.1: A schematic of satellite analysis

3.2 Topography Analysis

3.2.1 Extraction of Buildings' Coordinates

All the coordinates for the registered buildings were collected from a publicly available database provided by Statistics Canada [93]. The dataset includes information on the location of each building as a Shape File. In Figure 3.2, all the registered buildings are visualized on a map. The Kinsmen Sport Center Building is highlighted with a red marker. It is important to mention that a rotation of 19-degrees was applied to the coordinates to align them with the orientation of the map, which differs from the satellite image. This adjustment is necessary due to the distinct map projection employed by Google Maps. Therefore, a comparative analysis of two points, one from the dataset and the other from Google Maps, determined that an approximate 19-degree rotation aligns the coordinates with the projection used by Google Maps. Figure 3.3a shows the plotted geometry of the Kinsmen Sport Center Building. By rotating the coordinates by 19 degrees, the outer layer of the designated building was superimposed on Google Maps using the "gmplot" library [94] (seen in Figure 3.3b).

In order to map the building's edges on Google Maps, it was necessary to convert the distance from the center of the building to its edges and the bearing angle ϕ (the angle between the center of the building and each edge point) into latitude and longitude coordinates on the Earth's surface. Therefore, Equations 3.1 and 3.2 are used for the conversion.

$$\text{Latitudes} = \sin^{-1}\left(\sin(\alpha)\times\cos\left(\frac{\Delta}{R}\right)+\cos(\alpha)\times\sin\left(\frac{\Delta}{R}\right)\times\cos(\phi)\right) \tag{3.1}$$

$$\begin{aligned}\text{Longitudes} = \beta + \text{atan2d}\Bigg(&\sin(\phi)\times\sin\left(\frac{\Delta}{R}\right)\times\cos(\alpha),\\ &\cos\left(\frac{\Delta}{R}\right)-\sin(\alpha)\times\sin(\text{Latitudes})\Bigg)\end{aligned} \tag{3.2}$$

where the $R = 6371000$ represents the approximate average radius of the Earth in meters. α and β are the latitude and longitude of the center of the building, respectively. Δ is the relative location of the edge of the building with respect to the center of it.

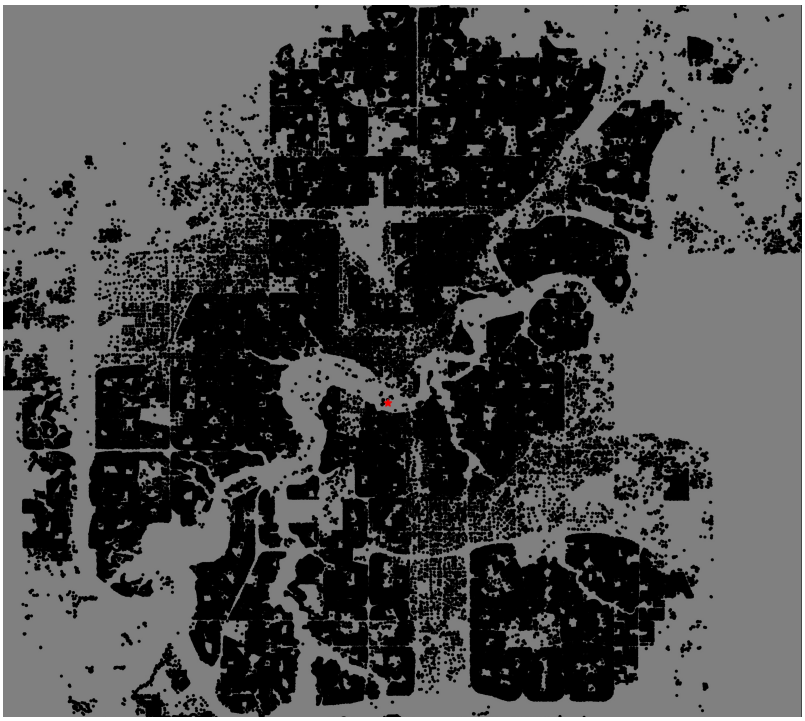

Figure 3.2: Location of all the registered buildings in the city of Edmonton; location of Kinsmen Sport Center with a red marker

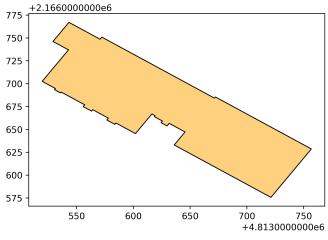

(a) Plot of building

(b) Rotating the coordinates and overlaying on Google Maps

Figure 3.3: Kinsmen Sport Center Building; (a) plotted geometry; (b) layout the plot on Google Maps, Maxar Technologies, Map data ©2022

3.2.2 Slope Analysis

Initially, the topographic details of the entire city of Edmonton are obtained from the publicly accessible CanVec Series database [95] administered by the Government of Canada. The resulting elevation map of Edmonton can be observed in Figure 3.4.

Once the elevation data points are acquired, the percent ground slope is calculated according to the guidelines outlined in the National Guide for Wildland-Urban Interface Fires [20]. This calculation is performed using Equation 3.3. This parameter is employed to adjust the ignition or priority zones encompassing the building (see Section 3.2.3), which necessitates fuel treatment measures to mitigate the risk of wildfires spreading and causing harm to the structure.

$$\% \text{ Ground Slope} = \frac{\text{Elevation}}{\text{Horizontal Ground Distance}} \times 100 \tag{3.3}$$

It is important to note that the ground slope can exceed 100% when the vertical elevation change surpasses the horizontal ground distance, indicating a slope steeper than 45 degrees. The topographic map and the corresponding percent ground slope of the vicinity surrounding the Kinsmen Sport Center Building are depicted in Figures 3.5.

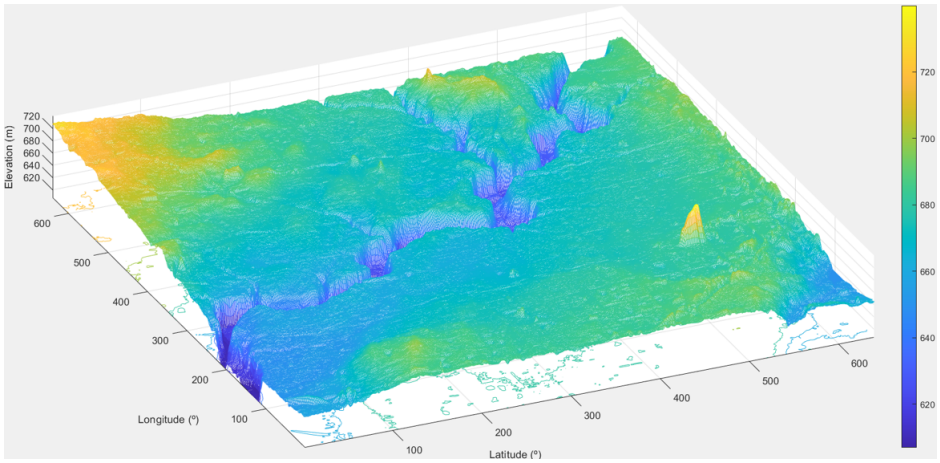

Figure 3.4: Elevation map of Edmonton city

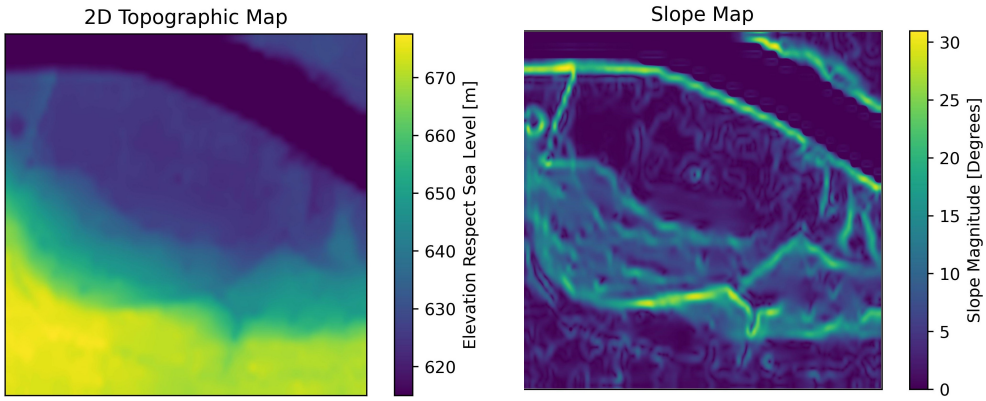

(a) Height map

(b) Slope magnitude map

Figure 3.5: Topographic map around the Kinsmen Sport Center Building

3.2.3 Ignition Zones

As described in Section 2.3.1, the management of fuel in designated areas surrounding structures, referred to as Priority Zones, is crucial. These Priority Zones are defined by a specific radius around the structure in accordance with National Guide for Wildland-Urban Interface Fire [20].

The first priority zone, spanning from 0 to 10 meters around the building, includes a non-combustible zone of 1.5 meters. Within this zone, fire-resistant vegetation should be present, while removing potential fuel sources such as mulch and wooden debris. Cured grass should be regularly trimmed to reduce the risk of ignition and fire intensity. Moving outward, the second priority zone stretches from 10 to 30 meters. In this area, trees should be pruned, with branches cut at least 2 meters from the ground and spaced at least 3 meters apart. Dry grass, debris, and needles should be consistently cleared. Lastly, the third priority zone covers the range of 30 to 100 meters and necessitates the inclusion of fire breaks between trees and other potentially flammable vegetation [20].

The process of determining the priority zones involves a series of steps. Firstly, it is necessary to locate the particular building of interest, in this case, the Kinsmen Sport Center Building, as detailed in Section 3.2.1 of the study. This building serves as the focal point for the subsequent analysis. The next step entails the ap-

plication of morphological dilation, a mathematical operation, which generates a buffer zone around the building. This buffer zone represents the extent of the priority zones associated with the structure. By enlarging the area around the building, the priority zones are effectively defined and demarcated. The generated buffer zone, encompassing the priority zones provides a clear representation of the spatial distribution.

Morphological dilation is a commonly utilized technique in image processing to enlarge objects or regions of interest. It involves adding pixels to the boundaries of objects using a predefined structuring element. By iteratively applying the structuring element to each pixel, overlapping areas with objects are expanded. This process is repeated for every pixel, resulting in an enlarged representation of the original objects [96]. Figure 3.6 presents a simplified schematic procedure of morphological dilation. In the context of identifying priority zones around buildings, morphological dilation is employed to create a buffer area surrounding the target building. This buffer area encompasses the desired priority zones, allowing for effective analysis and planning in fire prevention and management strategies.

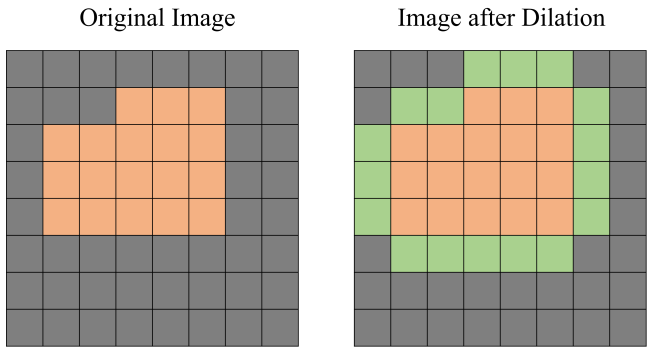

Figure 3.6: Schematic procedure of morphological dilation

The adjustment of priority zones is necessary, taking into account the surrounding slope, as topography plays a crucial role in the propagation of fires. According to the National Guide for Wildland-Urban Interface Fire [20], modifications to the second and third priority zones should be made based on the slope conditions in the following manner.

1. If the slope within the 2nd and 3rd priority zone falls between 30% and 55% (inclusive), the following adjustments should be made:
   (a) The priority zones should be expanded by a factor of 2 in the downward direction:
      i. The 2nd zone is extended from 30 to 60 meters.
      ii. The 3rd zone is extended from 100 to 200 meters.
   (b) The priority zones should be expanded by a factor of 1.5 in the horizontal direction:
      i. The 2nd zone is extended from 30 to 45 meters.
      ii. The 3rd zone is extended from 100 to 150 meters.
2. In cases where the slope within the 2nd and 3rd priority zone exceeds 55%, the following adjustments should be implemented:
   (a) The priority zones should be expanded by a factor of 4 in the downward direction:
      i. The 2nd zone is extended from 30 to 120 meters.
      ii. The 3rd zone is extended from 100 to 400 meters.
   (b) The priority zones should be expanded by a factor of 2 in the horizontal direction:
      i. The 2nd zone is extended from 30 to 60 meters.
      ii. The 3rd zone is extended from 100 to 200 meters.

The left side of Figure 3.7 illustrates the slope adjacent to the Kinsmen Building neighborhood, while the right side represents the slope falling within the specified ranges mentioned earlier ($30\% \leq \text{slope} \leq 55\%$, and $\text{slope} > 55\%$).

In order to emphasize the criticality of slope adjustment for priority ignition zones, two illustrative examples are presented. The objective is to shed light on the significance of considering the slope factor in determining the extent of ignition zones, as outlined in the National Guide for Wildland-Urban Interface Fire [20].
The first example, illustrated in Figure 3.8, shows a detailed slope adjustment

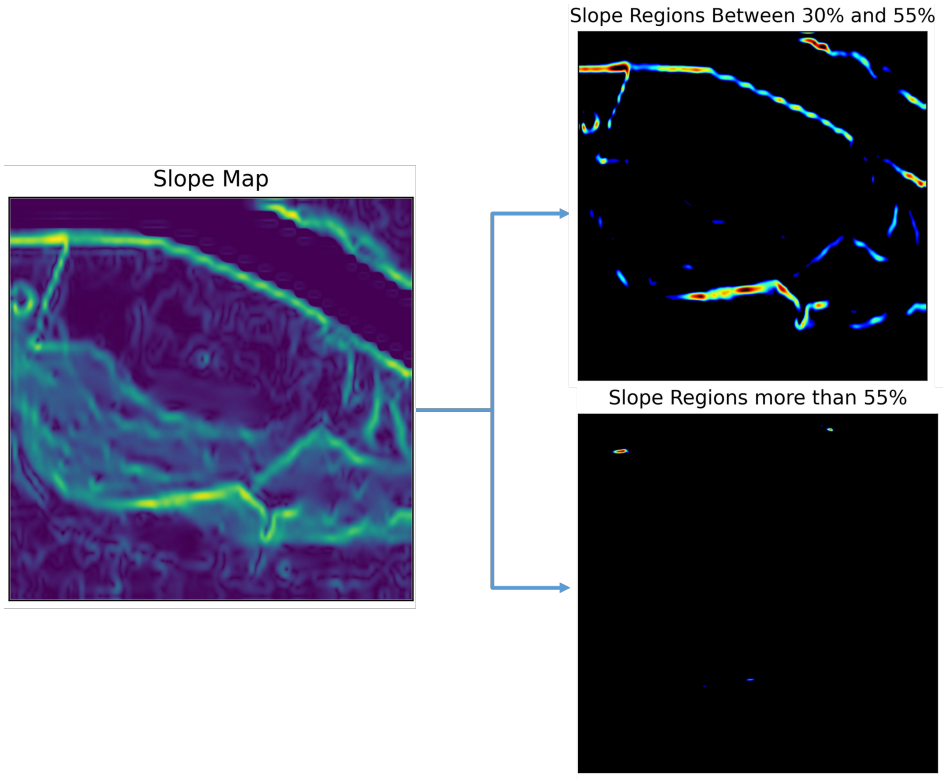

Figure 3.7: Adjustment of slope, (up-right) slope greater than 30% but less than 55%; (down-right) slope greater than 55%

analysis conducted on a randomly selected building situated in close proximity to high-slope regions. By examining the impact of slope on the spatial distribution of ignition zones, this example highlights the direct influence of slope conditions on the expansion of these zones. This analysis serves as a practical demonstration of how slope characteristics can significantly affect the determination of ignition zones, ensuring a more accurate assessment of potential exposure risks and enabling effective preventive measures.

Conversely, an additional example involves the examination of a building that is not in close proximity to any slope regions exceeding 30%. In this case, the West Edmonton Mall serves as a representative example. The purpose of this example is to demonstrate that when no significant slope is present in the vicinity, the adjusted ignition zones remain the same as the original zones. Figure 3.9 visually presents

this example.

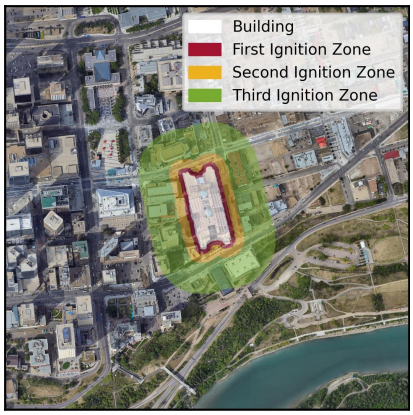

(a) Unadjusted ignition zones

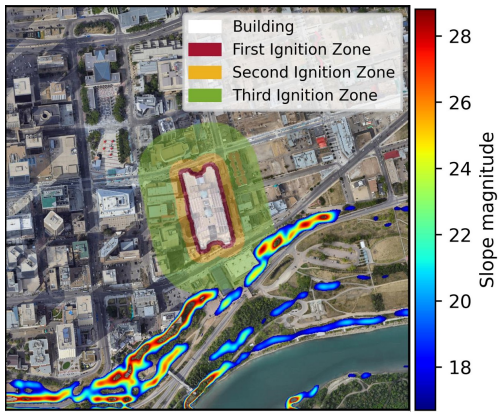

(b) Unadjusted ignition zones with slope regions between 30%-55%

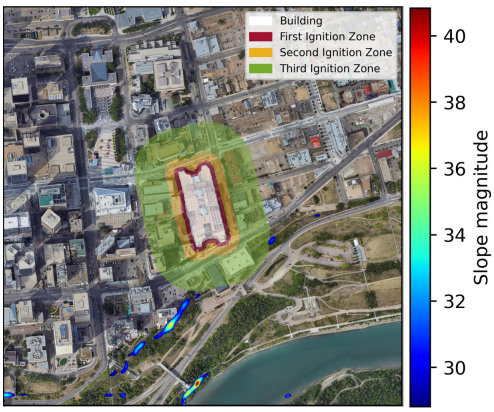

(c) Unadjusted ignition zones with slope regions greater than 55%

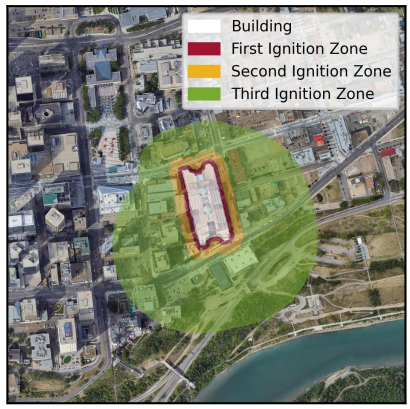

(d) Adjusted ignitions zones

Figure 3.8: Random building in a region with high slope

3.3 Tree and Grass Cover Semantic Segmentation

In this section, I employed the ResNet50 model to segment tree canopies such as conifers and deciduous trees, and surface fuels (grass) within the Kinsmen Sport Center region in Edmonton. This approach was chosen to facilitate the mapping of fuel distribution in the vicinity. The canopy detection encompassed various types of tree cover present in the area. Satellite data from Google Maps was utilized for

(a) Unadjusted ignition zones

(b) Unadjusted ignition zones with slope regions between 30%-55%

(c) Unadjusted ignition zones with slope regions greater than 55%

(d) Adjusted ignitions zones

Figure 3.9: West Edmonton Mall Building

data gathering due to its convenient accessibility as well as its free data Python-based extractor. The objective of this undertaking was to generate hazard zone mappings surrounding the specific building.

3.3.1 Deciduous Canopy and Grass Cover Segmentation

Data Gathering and Labeling

To train the machine learning models, a total of 479 images were obtained from Google Maps, capturing various areas within the city of Edmonton. Each image had a pixel size of 640×640. In these sample images, the tree crowns, which include both deciduous and conifer trees, and grass (surface fuel) were manually delineated using Labelme software. Although no on-ground validation was conducted for this data, it is anticipated that the label accuracy is reasonably high due to the high resolution of the images. For the data preparation, the dataset was partitioned, as seen below, to enhance the performance of the machine learning model. A major portion, 70%, was assigned to training, enabling the model to identify patterns and relationships in the data. To mitigate overfitting and refine the model's parameters, 20% of the dataset was dedicated to validation. This validation phase is vital for impartially assessing the model's fit during training, allowing for necessary modifications prior to the final assessment. The remaining 10% was used for testing, which is essential in providing a neutral evaluation of the model's efficiency on a separate dataset, demonstrating its potential to adapt to unfamiliar data. The process assures not just the model's accuracy on training data but also its effectiveness and dependability for an unseen dataset.

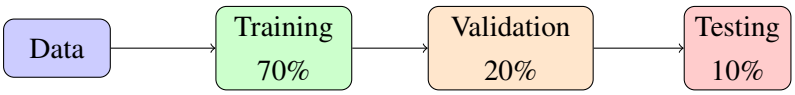

The outlined polygons were transformed into masks with the label "canopy" and "surfacefuels". Whatever remains, excluding canopy and surfacefuels, is a void mask. In the context of image processing and computer vision, a mask is a binary image (the value of 1 represents the foreground, and the value of 0 represents the background) that serves as a visual representation of certain regions or objects of interest within an image. It is commonly used for tasks like segmentation, where the goal is to separate specific objects or areas from the background. Figure 3.10 illustrates an example of a couple of randomly selected images alongside their corresponding masks. All the training dataset along with their masks are stored in a publicly available repository [97].

An image augmentation strategy employed in the dataset preparation is provided.

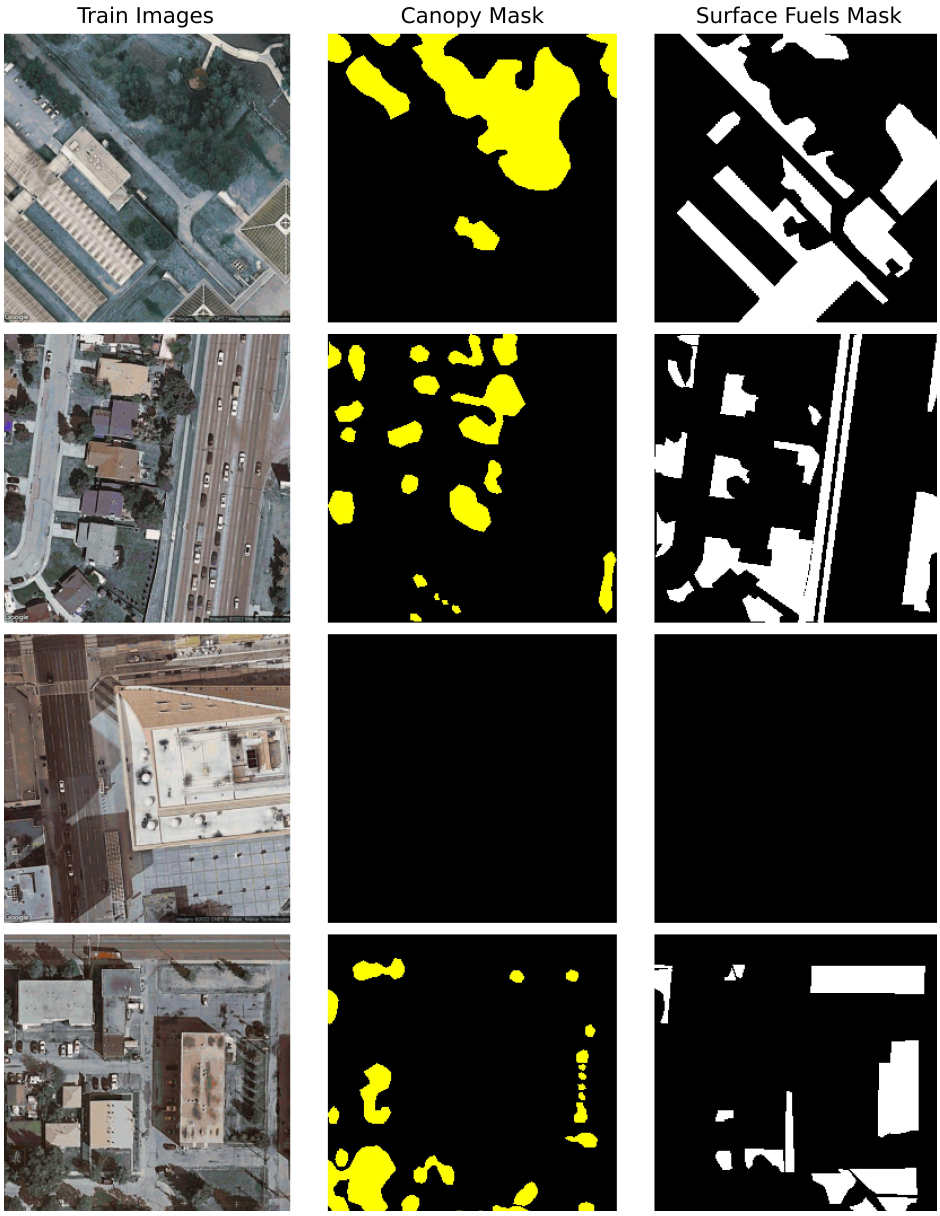

Figure 3.10: Randomly selected images with their corresponding masks that include two classes

This augmentation process is a crucial step in enhancing the robustness and generalizability of the machine learning model. The augmentation strategy involves randomly applying various transformations to the images and their corresponding masks in the dataset. These transformations can include changes in orientation (like rotations and flips). The augmentation is applied conditionally, meaning that not every image-mask pair undergoes these transformations. This approach ensures a balanced mix of original and augmented data, providing the model with a diverse and comprehensive learning experience.

Segmentation Model

In this section, I will delve into the models utilized in this study. The computer experiments involve two primary tasks: classification and semantic segmentation. In the classification task, an entire image is assigned a specific class, while in the segmentation task, each pixel is assigned a class. To tackle these tasks, I will employ CNNs constructed with the building blocks outlined in the theory section. Specifically, I will utilize the ResNet50 architecture [35] for semantic segmentation as well as classification.

ResNet50:

In the methodology section of this thesis, the model architecture chosen for the study is the ResNet50 [35], a CNN known for its depth and effectiveness in image classification tasks. The ResNet50 model, renowned for its 50-layer structure, is utilized here as a pre-trained encoder within a Feature Pyramid Network (FPN) segmentation model. This model is pre-trained with weights from ImageNet, a large and diverse visual database often used for enhancing the accuracy of visual recognition tasks.
Along with adapting the ResNet50 model for segmentation, a crucial aspect of the methodology was hyperparameter tuning to optimize the model's performance. Hyperparameter tuning involved adjusting various parameters such as the activation function, batch size, loss computation, learning rate, the number of epochs, and the learning rate drop factor, which are explained subsequently, to find the most effective combination for the task.

The segmentation model employs the 'softmax2d' activation function, which is particularly suitable for classifying each pixel in image data into distinct categories. For the management of training and validation datasets, DataLoaders are implemented with a configured batch size of 8, and shuffling is enabled to ensure a diverse set of data in each training batch. The loss computation for the model is conducted using the Cross-Entropy Loss function, which is adapted with class weights to address imbalances in the dataset effectively. The initial learning rate was set to 0.001, a critical parameter in controlling the rate at which the model learns. The learning rate drop strategy involved reducing the learning rate by a factor of 0.5 periodically, to fine-tune the convergence. This approach is effective in making smaller adjustments as the model gets closer to the optimal solution, preventing overshooting. The Adam optimizer was utilized for adjusting the weights of the network, known for its efficiency in handling large datasets and complex architectures. The model training spanned 40 epochs, where an epoch represents a complete pass through the entire training dataset. This duration was chosen to allow sufficient time for the model to learn and adjust its parameters. Each epoch involved training the model with the training dataset and validating its performance using a separate validation dataset.

3.3.2 Conifer Cover Segmentation

The segmentation of the conifer canopy is addressed separately due to differences in the data collection process compared to the previous section.

Data Gathering and Labeling

The process of collecting data for conifer canopies differs from the earlier section, which focused on deciduous trees and surface fuel. The previous section's data was sourced using Python scripts and the Google Maps API key, centered around Google Maps satellite images taken during seasons of lush vegetation like spring or summer. These images captured all forms of vegetation, including conifers, which posed a challenge in distinguishing conifer canopies from deciduous ones, particularly in densely vegetated zones. As highlighted in Section 2.3, the fire behavior varies between coniferous and deciduous vegetation. This necessitated

creating separate maps for each tree type to generate a comprehensive wildfire hazard map. One approach to discern conifer canopies in satellite pictures involves using wintertime shots. During this season, deciduous trees are leafless, whereas conifers remain green and easily identifiable. Python-based extraction of historical satellite data from the Google Earth engine is feasible using the Sentinel-2 satellite. However, its resolution is not suitable for the objective, as illustrated in Figure 3.11. To secure higher resolution images, Google Earth Pro, which grants access to historical data from commercial satellite providers like DigitalGlobe and Airbus, becomes an option. Yet, the satellite imagery obtained this way is not open for programmatic extraction due to licensing restrictions. Consequently, I manually extracted 80 images from the Google Earth Pro application centered on Edmonton City. These images, sized 1485X904 pixels and dated March 2022, contain conifer canopies intended for segmentation. The subsequent steps, including image preparation for the training set and mask set, align with the previous section, with a notable exception; there are only two single masks, the canopy mask and void mask (whatever is not canopy). Figure 3.12 illustrates an example of a couple of randomly selected images alongside their corresponding conifer mask. All the training dataset along with their masks are stored in a publicly available repository [97].

Figure 3.11: Winter satellite image of Edmonton using Sentinel-2 satellite; date: 02/2023

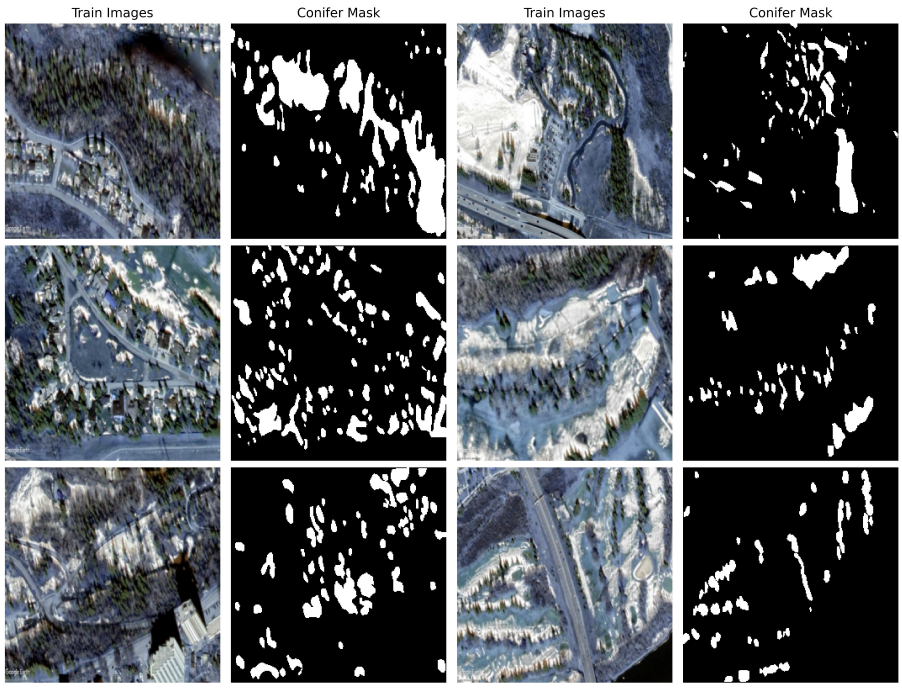

Figure 3.12: Conifer cover; randomly selected images with their corresponding masks

Segmentation Model

The CNN model employed for segmenting and classifying winter satellite images is identical to the model utilized for summer satellite imagery analysis. However, with the introduction of a new training dataset comprising winter satellite imagery, minor adjustments were made to the hyperparameter tuning process. Initially, the alteration involved changing the number of classes for the activation function from three to two. Moreover, given that the winter satellite images have a higher resolution compared to the summer images, the batch size has been decreased to four. This modification is designed to counterbalance the limited RAM availability during the model's training phase.

3.3.3 Model verification

To verify the results from the semantic segmentation, the region within the three ignition zones near the Kinsmen Sport Centre building was manually annotated

(referred to as the ”true label”), utilizing the Google Pro engine as a basis for this process. Due to the difficulty in distinguishing conifer trees from deciduous ones in satellite images, which makes manual labeling challenging, UAV photos captured during winter were utilized. The coordinates of each conifer tree were gathered from these photos to aid in accurately identifying and labeling conifer trees. Afterward, two methods can be employed to assess the accuracy of the semantic segmentation:

Comparison of binary masks (Regular accuracy)

The method involves converting both the true and detected masks to binary forms in pixel scaling and measuring the true positives (TP), where both masks have the same class. The accuracy can be determined as follows:

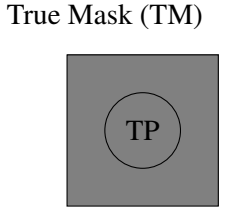

Accuracy = Area of TP / Total Area of TM

Intersection over Union (IoU)

This method measures the IoU by dividing the area of overlap between the true mask and the detected mask by the area covered by either of the masks (union) and penalizing false positives. The IoU can be determined as follows:

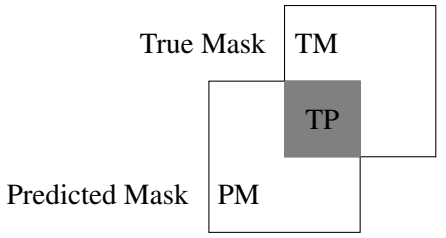

IoU = Area of TP / Area of (TM ∪ PM)

3.4 Integration of Topography Analysis and Vegetation Segmentation

After the CNN-based detection and segmentation of deciduous, coniferous, and grass-covered regions, the next step involves quantifying the extent of each fuel category (deciduous, coniferous, and grass-covered) within the defined three ignition zones, as outlined in Section 3.2.3. This information is crucial for exposure assessment of the risk of wildfire to a location/building, as stated in Table 2.2.
An example of topography analysis integration with vegetation segmentation can be seen in Figure 3.13. The fuel type, tree canopies and grass, are detected within the three slope-adjusted ignition zones of two random buildings in the City of Edmonton.

The type of fuel in each ignition zone of the building can be identified using Table 2.1 guidance. Subsequently, referring to Table 2.2, it is possible to assess the exposure level based on the fuel type in each ignition zone. The exposure level can reflect the likelihood of a potential fire spreading to and coming into contact with the structure.

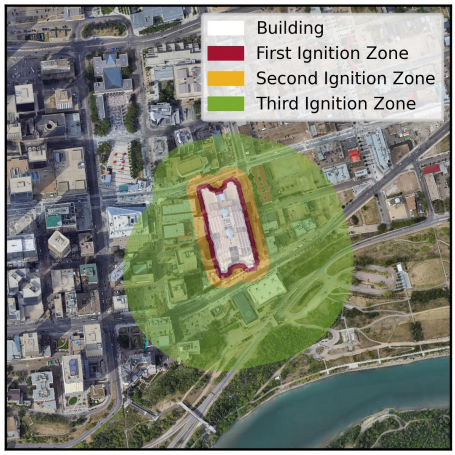

(a) Adjusted ignition zone of a building

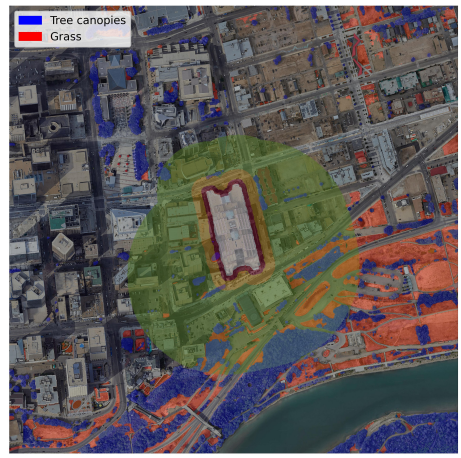

(b) Fuel map within the ignition zones

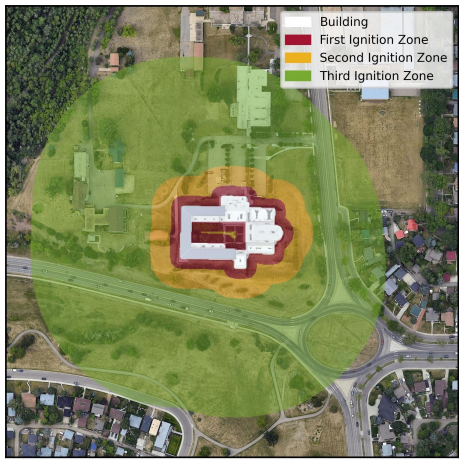

(c) Adjusted ignition zone of a building

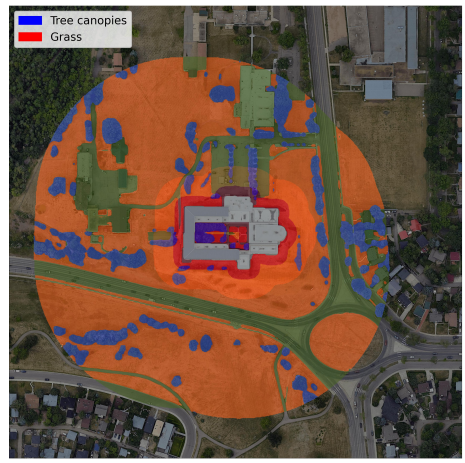

(d) Fuel map within the ignition zones

Figure 3.13: Fuel map within the ignition zones

Chapter 4

Results and Discussions

4.1 Ignition Zones

Based on the information provided in section 3.2.3, three ignition zones surrounding the Kinsmen Sport Center Building were identified and visualized in Figure 4.1. It should be emphasized that the figure represents the ignition zones without taking the slope into account. Consequently, the first, second, and third ignition zones are defined as spanning 0-10 meters, 10-30 meters, and 30-100 meters, respectively. Upon initial observation, it becomes evident that the third zone encompasses a combination of trees and grass, highlighting the need to incorporate fire breaks between the trees and other vegetation that may be prone to catching fire.

As per the guidelines provided in the National Guide for Wildland-Urban Interface Fire [20], adjustments to the second and third priority zones need to be made based on the slope conditions outlined in Section 3.2.3. Specifically, when considering slope regions ranging from 30% to 55%, Figure 4.2a shows the overlay of these regions on the corresponding Google image, highlighting the areas on the map where the slope falls within the specified range. Figure 4.2 provides a visual comparison between the unadjusted slope and the adjusted ignition zones.

In aligning with the National guideline [20], it's crucial to account for the impact of both upslope and downslope orientations. For instances where there's an upslope

Figure 4.1: Ignition zones around the Kinsmen Sport Center Building without slope adjustment

ranging from 30 to 55 percent towards a building, it's recommended to double the ignition zone in the direction of the slope and increase it by a factor of 1.5 in other horizontal directions. Conversely, in scenarios where the slope descends towards a building, the doubling factor in the slope's direction is not applicable, although an expansion by a factor of 1.5 is still advised in all directions. The rationale behind this lies in the behavior of fire on sloped terrain; fire tends to burn faster and more intensely uphill than on flat ground, leading to higher heat radiation. The inclination of the slope effectively brings the fuels on the upslope nearer to the flames, reducing the distance for energy transfer. This closer proximity enhances the 'view factor' for the fuels, allowing them to receive and absorb radiant energy more effectively, which preheats them prior to the flames' arrival. Consequently, this necessitates the expansion of the ignition zone to accommodate the heightened risk, explaining the increase of zone expansion in all directions with a factor of 1.5.

In Figure 4.3b, the regions with a slope greater than 55% are overlaid. It is evident that these regions, which fall outside the spanning area, do not impact the ignition zones. Therefore, the adjustment of the ignition zones was only based on the slope

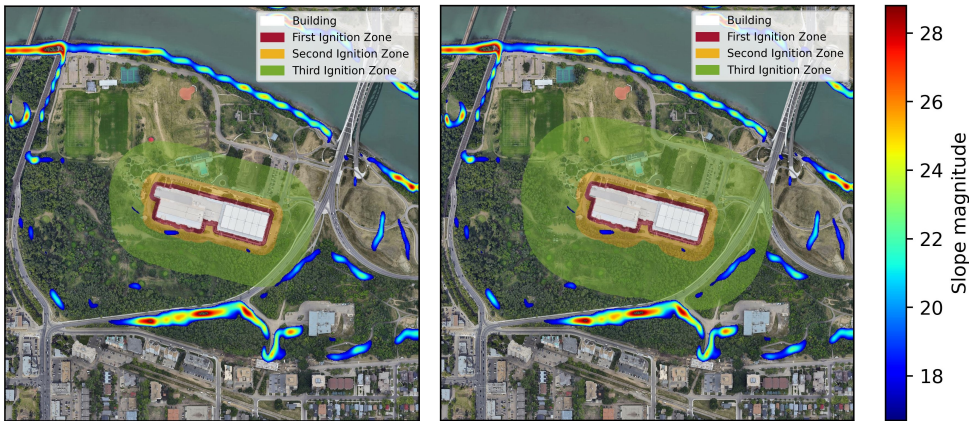

(a) Unadjusted ignition zones **(b)** Adjusted ignition zones

Figure 4.2: A comparison between the ignition zones when considering slope adjustment and when not considering slope adjustment. The focus is on slope regions ranging from 30% to 55%.

range of 30% to 55%.

(a) Unadjusted ignition zones **(b)** Adjusted ignition zones

Figure 4.3: A comparison between the ignition zones when considering slope adjustment and when not considering slope adjustment. The focus is on slope regions greater than 55%.

Figure 4.4a shows the overlay of the plotted Kinsmen Sport Center Building and the calculated ignition zones around it on Google Maps. On the other hand, Figure

4.4b demonstrates the same overlay with the adjusted slope, as discussed previously.

(a) Ignition zone map without slope adjustment **(b)** Ignition zone map with slope adjustment

Figure 4.4: Ignition zone map around Kinsmen Sport Center

4.2 Vegetation Segmentation and Integration with Topography Analysis

Figure 4.5 is a comparative visualization of fuel types, grass-cover and tree canopies, in the vicinity of the Kinsmen Sport Centre Building. Figure 4.5a shows the Masks of fuel where the colors blue and red are used to denote tree canopies and grass areas, respectively. This stylized map provides a clear and simplified view of the distribution of vegetation types that can contribute to fire fuel loads in the area. Figure 4.5b shows the 'Masks of fuel overlay on Google Maps', where the same color scheme is applied to an actual aerial image from Google Maps. This superimposition allows for a real-world correlation of the predictive mapping with the actual geographical layout surrounding the Kinsmen Sport Centre Building.

The detection and classification of the coniferous, deciduous, and grass-covered areas using the CNN within the priority zones of the Kinsmen Sport Centre Building is illustrated in Figure 4.6. It seems like that the grass-covered and deciduous ar-

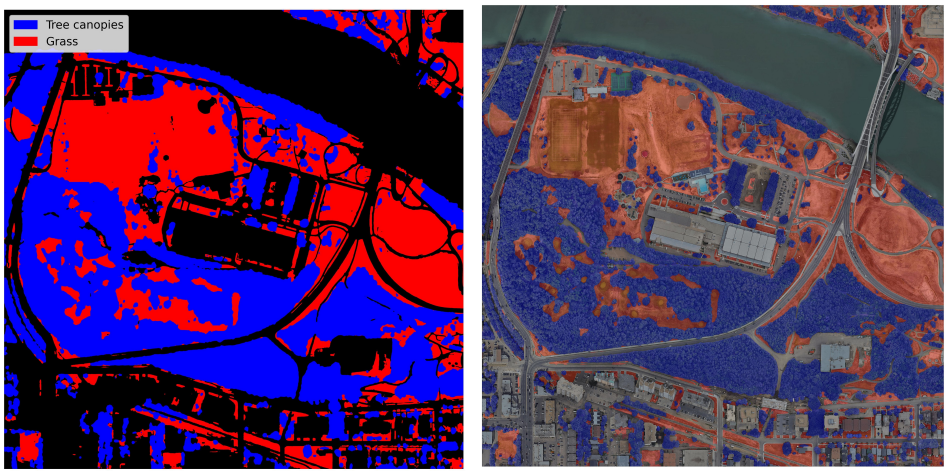

(a) Masks of fuel **(b)** Masks of fuel overlay on Google Maps

Figure 4.5: Prediction of fuels, including grass-cover and tree canopies, in the vicinity of Kinsmen Sport Centre Building

eas appear predominant, especially in open spaces around the building. Deciduous vegetation can be seen interspersed throughout the neighborhood, while coniferous trees are sporadically located, possibly in designated green zones and forest-like areas. Visual verification of detection in grassy regions may be straightforward, but identifying coniferous areas within dense vegetation from summer satellite captures is almost unfeasible. Yet, employing winter satellite imagery makes this task appear achievable.

The covered area and percentage of each fuel type in three ignition zones are shown in Table 4.1. The total vegetation coverage within ignition zones 1, 2, and 3 is 43%, 54%, and 75% of their respective total areas. In the entire ignition zones, the extent of deciduous canopy coverage surpasses that of grass-cover and coniferous canopies, establishing it as the primary fuel source for fire propagation. These findings can serve as a basis for measuring the fire exposure level from each fuel type near structures.

Table 2.1's fuel type category guideline, along with results from Table 4.1, were used to classify fuel types. For deciduous forests with less than 25% conifers, the fuel type is categorized as F1. This category also includes grass-cover. In ignition zones 2 and 3, due to the low presence of coniferous trees in tree canopies, the fuel

type is identified as F1. In ignition zone 1, although coniferous trees make up more than 25% of the canopies, the area is not forested, leading to the classification of the fuel type as ”continuous plant litter” (F1), according to the National guideline [20]. According to Table 2.2, the vegetation of ignition zone 1 (consisting of ”hazardous shrubs or trees”) has a high fire exposure level. The heat exposure level in ignition zone 2 is classified as low, primarily based on the fuel type category F1. While deciduous trees generally pose a lower fire risk, it is important to note the significant influence of conifers on the overall fire hazard due to their higher flammability. In the guideline [20], one critical factor in determining the risk level of a fuel category is the proportion of conifer trees present. In scenarios where conifer content exceeds 25 %, the risk is typically elevated due to the higher intensity and heat output of burning conifers. In the case of ignition zone 2, the conifer presence, though less than 25 %, still presents a notable risk factor, especially when in proximity to structures. The presence of any percentage of conifers near buildings should warrant attention, as their inherent flammability can significantly amplify the risk of fire spread and heat exposure. Therefore, while the overall classification of Ignition Zone 2 as a low-exposure area aligns with the guideline's criteria, it is important to acknowledge the potential for heightened risk posed by the presence of conifers, regardless of their proportion.
In ignition zone 3, the F1 fuel type, covering more than 50%, results in a high exposure classification. The fire exposure level map for the Kinsmen Sport Center Building is shown in Figure 4.7. This type of map can serve as a basis tool for understanding the spatial distribution of fire risks around any individual building.

The contribution of the mapping heat exposure level assessment using remote-sensing framework lies in bridging the gap between advanced remote-sensing technologies and practical wildfire risk assessment. By automating the WUI guideline notes [20] and utilizing satellite imagery, the methodology offers a faster, more efficient way to assess heat exposure risks. This is particularly crucial in regions prone to wildfires, where timely and accurate risk assessment can significantly impact prevention and mitigation strategies. As for the gaps in this field, one key area is the resolution limitation of satellite imagery, which may not capture fine details required for precise fuel type identification, and as a result, the outputs are mainly settled for large-scale assessment. The proposed tool, however, addresses this by

providing a rapid detailed fuel mapping through publicly available satellite imagery that can cover a large area at once and provide a micro-scaling assessment. Furthermore, implementing this method in a user-friendly application can enhance the accessibility of sophisticated wildfire risk assessment to a broader audience, including local governments, urban planners, and even homeowners, who may not have the expertise or resources to conduct detailed analyses.

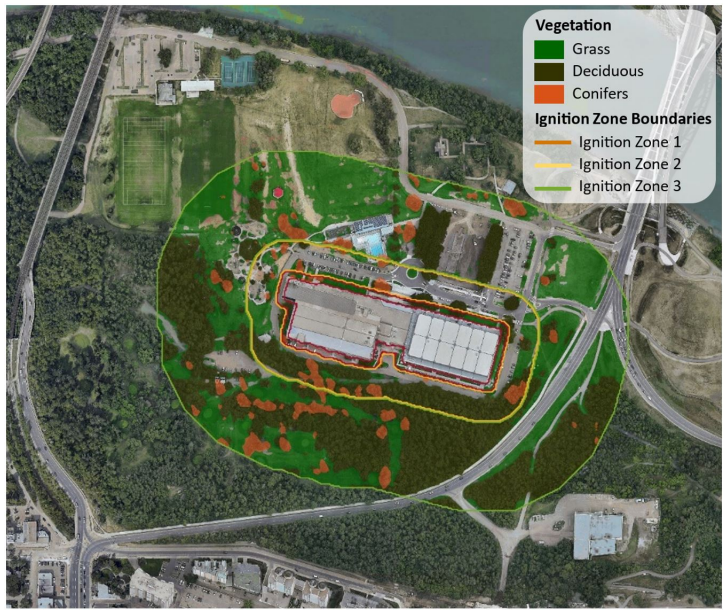

Figure 4.6: Classification of canopy and surface fuels for the Kinsmen Sport Center, overlaid with original image

Table 4.1: The amount of each fuel type in the ignition zones

Ignition Zone	Grass		Deciduous Tree		Coniferous Tree	
	Cover (%)	Area ($km^2 \times 10^{-3}$)	Cover (%)	Area ($km^2 \times 10^{-3}$)	Cover %	Area ($km^2 \times 10^{-3}$)
1	25	1.71	14	0.93	4	0.26
2	14	4.25	32	9.49	8	2.37
3	34	43.64	36	46.55	5	6.62

Table 4.2: Semantic segmentation verification results

Class	Accuracy (%)	IoU (%)
Grass	83.8	77.7
Conifer	81.8	61.2
Deciduous	95	88.7

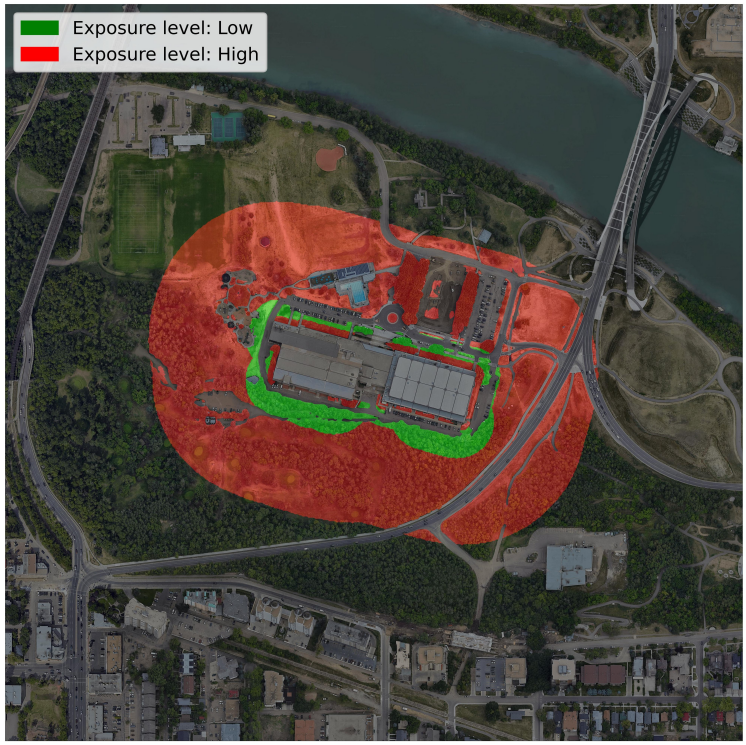

Figure 4.7: Map of exposure class within the ignition zones

4.3 Models Performance and Verification

Figures 4.8 and 4.9 illustrate the loss and accuracy metrics over each epoch for the segmentation of canopy/surface fuels (grass) and conifer canopies, respectively. The convergence trends of training and validation losses for both segmentation models imply effective generalization capabilities without indications of overfitting, as evidenced by the validation loss remaining consistent with the training loss. The parallelism of the trajectories between training and validation indicates

the notion of successful model generalization. The absence of overfitting is further supported by diminishing training losses and augmenting training accuracies, indicating that the models are adequately complex to handle the given segmentation tasks. No evidence of underfitting is present since the training losses decrease and the training accuracies increase, which suggests that the models' capacity is sufficient for the complexity of the tasks.

The validation accuracy and loss for the conifer canopy segmentation exhibit fluctuations, likely reflective of the diverse characteristics inherent to the validation dataset across different epochs. Furthermore, the batch-by-batch computation and subsequent averaging of validation loss and accuracy introduce an element of variability. Ideally, a larger batch size might have smoothed these trends, yet computational resource constraints necessitated a smaller batch size. Nevertheless, the model demonstrates decent accuracy, with no discernible signs of overfitting or underfitting.

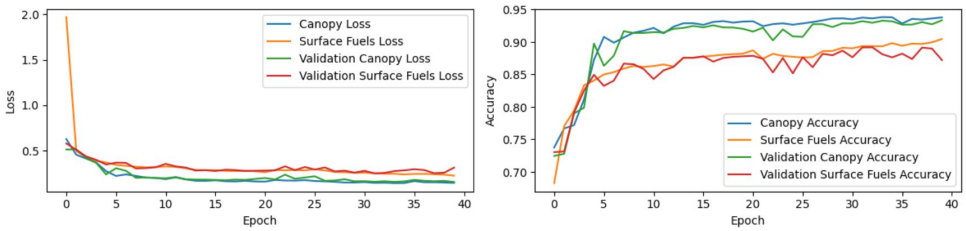

Figure 4.8: Loss and accuracy for the tree canopy and surface fuel (grass) segmentation task during training and validation phase

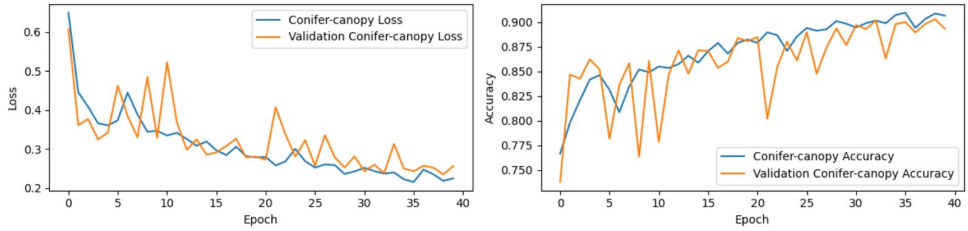

Figure 4.9: Loss and accuracy for the conifer segmentation task during training and validation phase

The model accuracy for the segmentation task was assessed based on the ground truth data (denoted as True mask) using regular accuracy and IoU methods. As

can be seen in table 4.2, for deciduous trees and grass, both methods obtained a relatively high accuracy level, indicating effective segmentation. However, for conifer trees, while the binary mask comparison showed reasonable accuracy, the IoU presented a lower value, underscoring the complexities involved in accurately segmenting this class. This issue is largely attributed to the quality of the training dataset. Although the resolution of the winter satellite images used for the segmentation of the conifer class was sufficient, the combination of the sun's positioning at that time of year and the satellite's image capture angle resulted in the presence of shadows (see Figure 3.12), which posed a significant challenge to effective detection. Addressing this challenge, one solution could be to utilize UAV photos taken during winter across the City of Edmonton for the training dataset. However, this approach necessitates substantial manual effort in managing and operating the system.

Supplementary figures (Figure 4.10 - 4.12) illustrate the mismatches in the masks between the detected and true labels for each class, offering a visual representation of the areas where segmentation was less accurate.

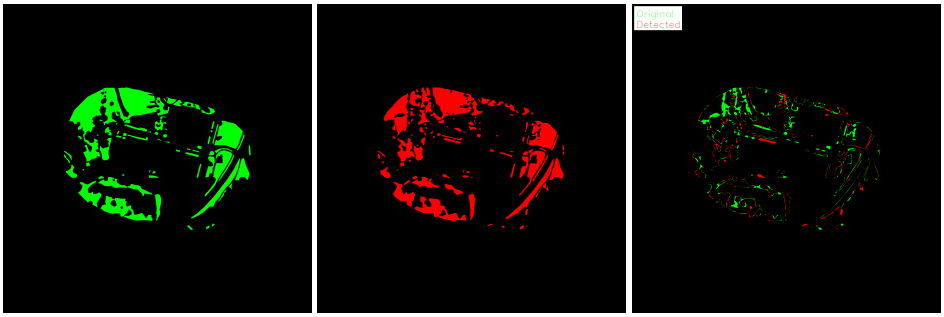

(a) True label **(b)** Detected **(c)** Mismatch

Figure 4.10: Validation for grass cover detection

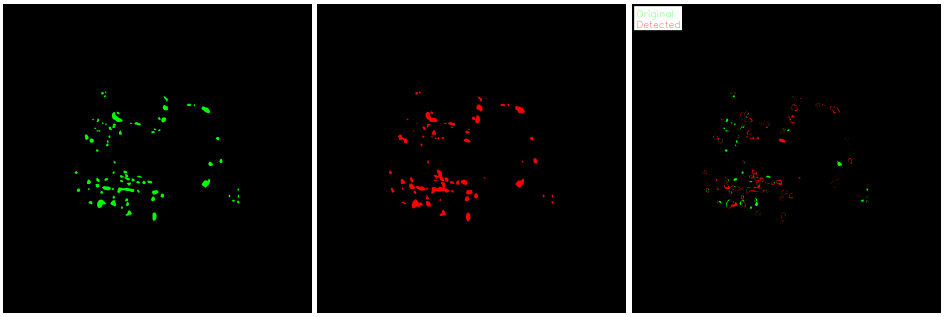

(a) True label **(b)** Detected **(c)** Mismatch

Figure 4.11: Validation for conifer cover detection

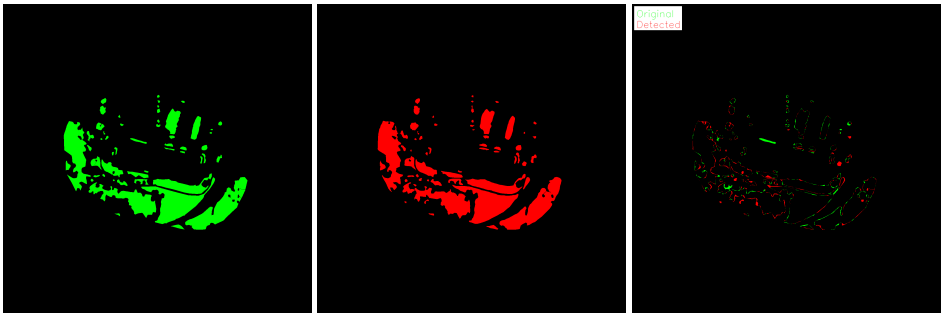

(a) True label **(b)** Detected **(c)** Mismatch

Figure 4.12: Validation for deciduous cover detection

Chapter 5

Conclusions and Future Work

Conclusions

A suite of methods was presented that is designed to extract specific information about the HIZ. As of today, several methods already exist in classifying fuel types in wildland areas for mapping hazard zones. This study focused on WUI regions to map the ignition zones around the vicinity of buildings to help mitigate the risk of fire exposure. The process of topography analysis began with locating the buildings of the entire city. Next, three priority zones with the adjustment of slope conditions in accordance with guidelines for WUI fires, were mapped around a building.

The topography analysis was followed by determining and classifying the fragmented or small forest vegetation area based on the different types of fuel categories stated in the FBP system by the application of CNNs. Satellite images during the summer were utilized to detect tree canopies and grass-covered areas. To overcome the challenge of detecting conifer trees among tree canopies, winter satellite images were used, as conifer foliage stands out distinctly among the leafless deciduous trees. The CNN model exhibited reasonable precision in the detection and classification of three vegetation categories. The accuracy of this model has the potential to be augmented with the expansion of the training dataset. Finally, the results from vegetation detection were combined with the topography

analysis to map the three ignition zones around a specific building.

This automated technique showed to have the potential to provide insights toward the risk of WUI fires and provide valuable opportunities, such as mapping the level of fire exposure, for decision-makers to mitigate fire hazards in urban areas.

Future work

The scope of this thesis has brought to light a number of areas that can benefit from further exploration in the realm of identifying fuels using satellite images for wildfire risk assessment in urban areas. A central focus should be on addressing the limitations and developing newer techniques for enhanced data accuracy.

Satellite images, while comprehensive, pose challenges in accurately identifying different fuels, determining the vertical size of fuels, consideration of seasonal changes such as the leafing of trees and the curing of grass, which are all essential characteristics in fire ignition and dynamic spread risk assessment. Therefore, to complement the satellite fuel detection and hazard analysis (that was investigated in this study), crowdsensing street-level methodology could be incorporated in.

- Street-level Crowdsensing: To bridge the data gaps left by satellite imagery, future studies should explore the potential of street-level crowdsensing. Videos from car-mounted cameras can offer details of fuel characteristics. For instance:
  - CNNs can be employed to identify the type of fuel, the seasonal changes in deciduous trees, and the curing stage of grass.
  - Incorporating Global Navigation Satellite Systems (GNSS) in cameras like GoPro™ can be instrumental in estimating the crown base height of conifers, a crucial parameter for fire behavior analysis. The principle behind this is based on perspective distortion where objects appear smaller or larger based on distance. With a moving vehicle, this can be used to determine the dimensions of objects from video frames.
  - CNN models can segment grass cover and then determine its curing state by analyzing the greenery factor using color analysis techniques.

Street-level crowdsensing is not without limitations. Its scope is restricted to areas along roads, neglecting interiors of forested and parkland regions devoid of road access. Thereby, there is a need to integrate the large-scale but low-detailed satellite analysis with the small-scale but high-detailed crowdsensing information to have a more precise updated understanding of the fire risk for wildfire in urban areas.

Fire behavior, as defined by the FBP system, hinges on factors like Rate of Spread (which is the number of meters consumed by the fire per minute (m/min)) and Head Fire Intensity (which is the amount of energy released per meter progress of the fire front line per second and is often reported in kW/m). Understanding these parameters demands more detailed mapping. By considering both satellite and crowdsensing data, a comprehensive picture of potential fire risks can be painted, potentially saving habitats and urban landscapes from the devastating impacts of wildfires.

Bibliography

[1] E. J. Bush, J. W. Loder, T. S. James, L. D. Mortsch, and S. J. Cohen, "An overview of canada's changing climate," *Canada in a changing climate: Sector perspectives on impacts and adaptation*, pp. 23–64, 2014.

[2] M. C. Kirchmeier-Young, N. P. Gillett, F. W. Zwiers, A. J. Cannon, and F. Anslow, "Attribution of the influence of human-induced climate change on an extreme fire season," *Earth's Future*, vol. 7, no. 1, pp. 2–10, 2019.

[3] M. D. Flannigan, M. A. Krawchuk, W. J. de Groot, B. M. Wotton, and L. M. Gowman, "Implications of changing climate for global wildland fire," *International journal of wildland fire*, vol. 18, no. 5, pp. 483–507, 2009.

[4] B. M. Wotton, C. A. Nock, and M. D. Flannigan, "Forest fire occurrence and climate change in canada," *International Journal of Wildland Fire*, vol. 19, no. 3, pp. 253–271, 2010.

[5] Global News, "Alberta wildfire season '10 times more severe' than recent averages, province says." globalnews.ca.

[6] E. Pasiuk, "Residents west of Edmonton under evacuation orders due to out-of-control wildfire." cbc.ca, 2023.

[7] A. Bar-Massada, V. C. Radeloff, and S. I. Stewart, "Biotic and abiotic effects of human settlements in the wildland–urban interface," *Bioscience*, vol. 64, no. 5, pp. 429–437, 2014.

[8] J. D. Cohen, “Preventing disaster: home ignitability in the wildland-urban interface,” *Journal of forestry*, vol. 98, no. 3, pp. 15–21, 2000.

[9] C. Lampin-Maillet, M. Jappiot, M. Long, D. Morge, and J.-P. Ferrier, “Characterization and mapping of dwelling types for forest fire prevention,” *Computers, Environment and urban systems*, vol. 33, no. 3, pp. 224–232, 2009.

[10] J. Cohen and A. Westhaver, “An examination of the lytton, british columbia wildland-urban fire destruction: summary report to the british columbia firesmart committee,” *Institute for Catastrophic Loss Reduction*, 2022.

[11] S. S. Schulze, E. C. Fischer, S. Hamideh, and H. Mahmoud, “Wildfire impacts on schools and hospitals following the 2018 california camp fire,” *Natural Hazards*, vol. 104, pp. 901–925, 2020.

[12] A. B. Massada, V. C. Radeloff, S. I. Stewart, and T. J. Hawbaker, “Wildfire risk in the wildland–urban interface: a simulation study in northwestern wisconsin,” *Forest Ecology and Management*, vol. 258, no. 9, pp. 1990–1999, 2009.

[13] G. Herrero-Corral, M. Jappiot, C. Bouillon, and M. Long-Fournel, “Application of a geographical assessment method for the characterization of wildland–urban interfaces in the context of wildfire prevention: A case study in western madrid,” *Applied Geography*, vol. 35, no. 1-2, pp. 60–70, 2012.

[14] J. K. Lein and N. I. Stump, “Assessing wildfire potential within the wildland–urban interface: A southeastern ohio example,” *Applied Geography*, vol. 29, no. 1, pp. 21–34, 2009.

[15] J. Cohen, “The wildland-urban interface fire problem. forest history today,” *Fall*, vol. 2008, pp. 20–26, 2008.

[16] J. D. Cohen, “Wildland–urban fire—a different approach,” *Proceedings of the Firefigther Safety Summit, International Association of Wildland Fire, Missoula, MT, November*, pp. 6–8, 2001.

[17] J. D. Cohen and B. W. Butler, “Modeling potential structure ignitions from flame radiation exposure with implications for wildland/urban interface fire

management," in *Thirteenth Fire and Forest Meteorology Conference, Lorne, Australia*, p. 82, 1996.

[18] A. A. Ager, N. M. Vaillant, and M. A. Finney, "A comparison of landscape fuel treatment strategies to mitigate wildland fire risk in the urban interface and preserve old forest structure," *Forest Ecology and Management*, vol. 259, no. 8, pp. 1556–1570, 2010.

[19] J. D. Cohen, "A site-specific approach for assessing the fire risk to structures at the wildland/urban interface," in *Fire and the Environment: Ecological and Cultural Perspectives: Proceedings of an International Symposium, Knoxville, Tennessee, March 20-24, 1990*, vol. 69, p. 252, Southeastern Forest Experiment Station, 1991.

[20] N. Bénichou, M. Adelzadeh, J. Singh, I. Gomaa, N. Elsagan, M. T. Kinateder, C. Ma, A. Gaur, A. C. Bwalya, and M. A. Sultan, *National Guide for Wildland-urban interface fires: guidance on hazard and exposure assessment, property protection, community resilience and emergency planning to minimize the impact of wildland-urban interface fires*. National Research Council Canada, 2021.

[21] K. Johansen, N. C. Coops, S. E. Gergel, and Y. Stange, "Application of high spatial resolution satellite imagery for riparian and forest ecosystem classification," *Remote sensing of Environment*, vol. 110, no. 1, pp. 29–44, 2007.

[22] T. R. Tooke, N. C. Coops, N. R. Goodwin, and J. A. Voogt, "Extracting urban vegetation characteristics using spectral mixture analysis and decision tree classifications," *Remote Sensing of Environment*, vol. 113, no. 2, pp. 398–407, 2009.

[23] P. Roy, M. Behera, and S. Srivastav, "Satellite remote sensing: sensors, applications and techniques," *Proceedings of the National Academy of Sciences, India Section A: Physical Sciences*, vol. 87, pp. 465–472, 2017.

[24] Z. Liu, X. Li, P. Luo, C.-C. Loy, and X. Tang, "Semantic image segmentation via deep parsing network," in *Proceedings of the IEEE international conference on computer vision*, pp. 1377–1385, 2015.

[25] W. Rawat and Z. Wang, "Deep convolutional neural networks for image classification: A comprehensive review," *Neural computation*, vol. 29, no. 9, pp. 2352–2449, 2017.

[26] Y. Chen, "Convolutional neural network for sentence classification," Master's thesis, University of Waterloo, 2015.

[27] Q. Feng, J. Liu, and J. Gong, "Uav remote sensing for urban vegetation mapping using random forest and texture analysis," *Remote sensing*, vol. 7, no. 1, pp. 1074–1094, 2015.

[28] E. F. Moran, "Land cover classification in a complex urban-rural landscape with quickbird imagery," *Photogrammetric engineering and remote sensing*, vol. 76, no. 10, p. 1159, 2010.

[29] "Google earth engine: A planetary-scale geospatial analysis platform." earthengine.google.com, 2015.

[30] "Google maps." wikipedia.org.

[31] "Electromagnetic spectrum– regions of interest to the chemical spectroscopist." universetoday.com.

[32] "Chlorophyll absorption spectrum." commons.wikimedia.org.

[33] Y. LeCun, Y. Bengio, and G. Hinton, "Deep learning," *nature*, vol. 521, no. 7553, pp. 436–444, 2015.

[34] G. Marcus, "Deep learning: A critical appraisal," *arXiv preprint arXiv:1801.00631*, 2018.

[35] K. He, X. Zhang, S. Ren, and J. Sun, "Deep residual learning for image recognition," in *Proceedings of the IEEE conference on computer vision and pattern recognition*, pp. 770–778, 2016.

[36] Richard Nagyfi, "The differences between artificial and biological neural networks." towardsdatascience.com.

[37] F. Rosenblatt, "The perceptron: a probabilistic model for information storage and organization in the brain.," *Psychological review*, vol. 65, no. 6, p. 386, 1958.

[38] Wikimedia Commons, "Convolution Animation." commons.wikimedia.org.

[39] V. Dumoulin and F. Visin, "A guide to convolution arithmetic for deep learning," *arXiv preprint arXiv:1603.07285*, 2016.

[40] I. Goodfellow, Y. Bengio, and A. Courville, *Deep learning*. MIT press, 2016.

[41] K. Fukushima, "Self-organizing multilayered neural network," *The Transactions of Electronics and communication Engineers D*, vol. 58, no. 9, p. 530, 1975.

[42] M. Bear, B. Connors, and M. A. Paradiso, *Neuroscience: exploring the brain, enhanced edition: exploring the brain*. Jones & Bartlett Learning, 2020.

[43] A. Krizhevsky, I. Sutskever, and G. E. Hinton, "Imagenet classification with deep convolutional neural networks," *Advances in neural information processing systems*, vol. 25, 2012.

[44] Environment and Sustainable Resource Development, Government of Alberta, "How different tree species impact the spread of wildfire." alberta.ca, 2012.

[45] C. E. Van Wagner, B. Stocks, B. Lawson, M. Alexander, T. Lynham, and R. McAlpine, "Development and structure of the canadian forest fire behavior prediction system," *Forestry Canada Fire Danger Group Information Report ST-X-3.(Ottawa, ON)*, 1992.

[46] N. Phelps, H. Cameron, A. M. Forbes, T. Schiks, D. Schroeder, and J. L. Beverly, "The alberta wildland fuels inventory program (awfip): data description and reference tables," *Annals of Forest Science*, vol. 79, no. 1, p. 28, 2022.

[47] FireSmart of Canada, "Home Ignition Zone." firesmartcanada.ca.

[48] NRC, *National Building Code of Canada*. National Research Council Canada, 2015.

[49] Canadian Council of Forest Ministers, "National Forestry Database." nfdp.ccfm.org, 2021.

[50] Natural Resources Canada, "Canadian Wildland Fire Information System." bit.ly, 2019.

[51] GloVis, "Usgs, global visualization viewer." glovis.usgs.gov.

[52] H. Hashim, Z. Abd Latif, and N. A. Adnan, "Urban vegetation classification with ndvi threshold value method with very high resolution (vhr) pleiades imagery," *The International Archives of the Photogrammetry, Remote Sensing and Spatial Information Sciences*, vol. 42, pp. 237–240, 2019.

[53] M. O. Idrees, D. M. Omar, A. Babalola, H. A. Ahmadu, A. Yusuf, and F. O. Lawal, "Urban land use land cover mapping in tropical savannah using landsat-8 derived normalized difference vegetation index (ndvi) threshold," *South African Journal of Geomatics*, vol. 11, no. 1, 2022.

[54] P. Gibbons, L. Van Bommel, A. M. Gill, G. J. Cary, D. A. Driscoll, R. A. Bradstock, E. Knight, M. A. Moritz, S. L. Stephens, and D. B. Lindenmayer, "Land management practices associated with house loss in wildfires," *PloS one*, vol. 7, no. 1, p. e29212, 2012.

[55] A. D. Syphard, J. E. Keeley, A. B. Massada, T. J. Brennan, and V. C. Radeloff, "Housing arrangement and location determine the likelihood of housing loss due to wildfire," *PloS one*, vol. 7, no. 3, p. e33954, 2012.

[56] J. L. Beverly, P. Bothwell, J. Conner, and E. Herd, "Assessing the exposure of the built environment to potential ignition sources generated from vegetative fuel," *International journal of wildland fire*, vol. 19, no. 3, pp. 299–313, 2010.

[57] U. Bhandary and B. Muller, "Land use planning and wildfire risk mitigation: an analysis of wildfire-burned subdivisions using high-resolution remote sensing imagery and gis data," *Journal of Environmental Planning and Management*, vol. 52, no. 7, pp. 939–955, 2009.

[58] R. V. Platt, "Wildfire hazard in the home ignition zone: An object-oriented analysis integrating lidar and vhr satellite imagery," *Applied Geography*, vol. 51, pp. 108–117, 2014.

[59] S. Réjichi and F. Chaâbane, "Svm spatio-temporal vegetation classification using hr satellite images," in *Sensors, Systems, and Next-Generation Satellites XV*, vol. 8176, pp. 521–534, SPIE, 2011.

[60] W. Wei, D. Polap, X. Li, M. Woźniak, and J. Liu, "Study on remote sensing image vegetation classification method based on decision tree classifier," in *2018 IEEE Symposium Series on Computational Intelligence (SSCI)*, pp. 2292–2297, IEEE, 2018.

[61] C. Zhang and Z. Xie, "Combining object-based texture measures with a neural network for vegetation mapping in the everglades from hyperspectral imagery," *Remote sensing of environment*, vol. 124, pp. 310–320, 2012.

[62] J. Tigges, T. Lakes, and P. Hostert, "Urban vegetation classification: Benefits of multitemporal rapideye satellite data," *Remote Sensing of environment*, vol. 136, pp. 66–75, 2013.

[63] S. H. Boles, X. Xiao, J. Liu, Q. Zhang, S. Munkhtuya, S. Chen, and D. Ojima, "Land cover characterization of temperate east asia using multi-temporal vegetation sensor data," *Remote Sensing of Environment*, vol. 90, no. 4, pp. 477–489, 2004.

[64] Z. Lv, Y. Hu, H. Zhong, J. Wu, B. Li, and H. Zhao, "Parallel k-means clustering of remote sensing images based on mapreduce," in *Web Information Systems and Mining: International Conference, WISM 2010, Sanya, China, October 23-24, 2010. Proceedings*, pp. 162–170, Springer, 2010.

[65] J. Y. Anchang, E. O. Ananga, and R. Pu, "An efficient unsupervised index based approach for mapping urban vegetation from ikonos imagery," *International Journal of Applied Earth Observation and Geoinformation*, vol. 50, pp. 211–220, 2016.

[66] A. Abdollahi, B. Pradhan, and A. M. Alamri, "An ensemble architecture of deep convolutional segnet and unet networks for building semantic segmentation from high-resolution aerial images," *Geocarto International*, vol. 37, no. 12, pp. 3355–3370, 2022.

[67] Y. Xie, H. Bao, S. Shekhar, and J. Knight, "A timber framework for mining urban tree inventories using remote sensing datasets," in *2018 IEEE International Conference on Data Mining (ICDM)*, pp. 1344–1349, IEEE, 2018.

[68] L. T. Waser, M. Küchler, K. Jütte, and T. Stampfer, "Evaluating the potential of worldview-2 data to classify tree species and different levels of ash mortality," *Remote Sensing*, vol. 6, no. 5, pp. 4515–4545, 2014.

[69] M. Immitzer, C. Atzberger, and T. Koukal, "Tree species classification with random forest using very high spatial resolution 8-band worldview-2 satellite data," *Remote sensing*, vol. 4, no. 9, pp. 2661–2693, 2012.

[70] C. Zhang, K. Xia, H. Feng, Y. Yang, and X. Du, "Tree species classification using deep learning and rgb optical images obtained by an unmanned aerial vehicle," *Journal of Forestry Research*, vol. 32, no. 5, pp. 1879–1888, 2021.

[71] A. Abdollahi and B. Pradhan, "Urban vegetation mapping from aerial imagery using explainable ai (xai)," *Sensors*, vol. 21, no. 14, p. 4738, 2021.

[72] Q. Chen, L. Wang, Y. Wu, G. Wu, Z. Guo, and S. Waslander, "Aerial imagery for roof segmentation: A large-scale dataset towards automatic mapping of buildings. arxiv 2018," *arXiv preprint arXiv:1807.09532*, 2018.

[73] S. M. Lundberg and S.-I. Lee, "A unified approach to interpreting model predictions," *Advances in neural information processing systems*, vol. 30, 2017.

[74] S. S. Matin and B. Pradhan, "Earthquake-induced building-damage mapping using explainable ai (xai)," *Sensors*, vol. 21, no. 13, p. 4489, 2021.

[75] R. Pu and S. Landry, "A comparative analysis of high spatial resolution ikonos and worldview-2 imagery for mapping urban tree species," *Remote Sensing of Environment*, vol. 124, pp. 516–533, 2012.

[76] P. Srestasathiern and P. Rakwatin, "Oil palm tree detection with high resolution multi-spectral satellite imagery," *Remote Sensing*, vol. 6, no. 10, pp. 9749–9774, 2014.

[77] D. Li, Y. Ke, H. Gong, and X. Li, "Object-based urban tree species classification using bi-temporal worldview-2 and worldview-3 images," *Remote Sensing*, vol. 7, no. 12, pp. 16917–16937, 2015.

[78] M. Rezaee, Y. Zhang, R. Mishra, F. Tong, and H. Tong, "Using a vgg-16 network for individual tree species detection with an object-based approach," in *2018 10th IAPR Workshop on Pattern Recognition in Remote Sensing (PRRS)*, pp. 1–7, IEEE, 2018.

[79] O. Nevalainen, E. Honkavaara, S. Tuominen, N. Viljanen, T. Hakala, X. Yu, J. Hyyppä, H. Saari, I. Pölönen, N. N. Imai, *et al.*, "Individual tree detection and classification with uav-based photogrammetric point clouds and hyperspectral imaging," *Remote Sensing*, vol. 9, no. 3, p. 185, 2017.

[80] A. B. Nielsen, J. Östberg, T. Delshammar, *et al.*, "Review of urban tree inventory methods used to collect data at single-tree level," *Arboriculture & Urban Forestry*, vol. 40, no. 2, pp. 96–111, 2014.

[81] P. Stubbings, J. Peskett, F. Rowe, and D. Arribas-Bel, "A hierarchical urban forest index using street-level imagery and deep learning," *Remote Sensing*, vol. 11, no. 12, p. 1395, 2019.

[82] S. Li, S. Dragicevic, F. A. Castro, M. Sester, S. Winter, A. Coltekin, C. Pettit, B. Jiang, J. Haworth, A. Stein, *et al.*, "Geospatial big data handling theory and methods: A review and research challenges," *ISPRS journal of Photogrammetry and Remote Sensing*, vol. 115, pp. 119–133, 2016.

[83] A. Berland and D. A. Lange, "Google street view shows promise for virtual street tree surveys," *Urban Forestry & Urban Greening*, vol. 21, pp. 11–15, 2017.

[84] L. Ma, Y. Liu, X. Zhang, Y. Ye, G. Yin, and B. A. Johnson, "Deep learning in remote sensing applications: A meta-analysis and review," *ISPRS journal of photogrammetry and remote sensing*, vol. 152, pp. 166–177, 2019.

[85] I. Seiferling, N. Naik, C. Ratti, and R. Proulx, "Green streets- quantifying and mapping urban trees with street-level imagery and computer vision," *Landscape and Urban Planning*, vol. 165, pp. 93–101, 2017.

[86] X. Li, C. Ratti, and I. Seiferling, "Mapping urban landscapes along streets using google street view," in *Advances in Cartography and GIScience: Selections from the International Cartographic Conference 2017 28*, pp. 341–356, Springer, 2017.

[87] D. Laumer, N. Lang, N. van Doorn, O. Mac Aodha, P. Perona, and J. D. Wegner, "Geocoding of trees from street addresses and street-level images," *ISPRS Journal of Photogrammetry and Remote Sensing*, vol. 162, pp. 125–136, 2020.

[88] J. D. Wegner, S. Branson, D. Hall, K. Schindler, and P. Perona, "Cataloging public objects using aerial and street-level images-urban trees," in *Proceedings of the IEEE Conference on Computer Vision and Pattern Recognition*, pp. 6014–6023, 2016.

[89] H. Zhao, J. Shi, X. Qi, X. Wang, and J. Jia, "Pyramid scene parsing network," in *Proceedings of the IEEE conference on computer vision and pattern recognition*, pp. 2881–2890, 2017.

[90] S. Tokui, K. Oono, S. Hido, and J. Clayton, "Chainer: a next-generation open source framework for deep learning," in *Proceedings of workshop on machine learning systems (LearningSys) in the twenty-ninth annual conference on neural information processing systems (NIPS)*, vol. 5, pp. 1–6, 2015.

[91] S. Lumnitz, T. Devisscher, J. R. Mayaud, V. Radic, N. C. Coops, and V. C. Griess, "Mapping trees along urban street networks with deep learning and street-level imagery," *ISPRS Journal of Photogrammetry and Remote Sensing*, vol. 175, pp. 144–157, 2021.

[92] C. Godard, O. Mac Aodha, and G. J. Brostow, "Unsupervised monocular depth estimation with left-right consistency," in *Proceedings of the IEEE conference on computer vision and pattern recognition*, pp. 270–279, 2017.

[93] Statistics Canada, “The Open Database of Buildings.” statcan.gc.ca, 2019.

[94] Pypi, “gmplot.” pypi.org.

[95] Natural Resources Canada, “Topographic Data of Canada - CanVec Series - Open Government Portal.” canada.ca, 2022.

[96] Sravan Danda, Aditya Challa B. S. Daya Sagar, “Morphological Dilation.” springer.com.

[97] Mohammad Afaghi, “Fuel Detection Training Dataset.” github.com/mafaghi.